2022-12

GAN LIGHT EMISSION CONTROLLED DC-DC CONVERTER

Johnston, Justin D.

Monterey, CA; Naval Postgraduate School

NAVAL POSTGRADUATE SCHOOL

MONTEREY, CALIFORNIA

THESIS

GAN LIGHT EMISSION CONTROLLED DC-DC CONVERTER

by

Justin D. Johnston

December 2022

Thesis Advisor:	Todd R. Weatherford
Co-Advisor:	Keith Corzine, UC Santa Cruz
Second Reader:	Matthew A. Porter

THIS PAGE INTENTIONALLY LEFT BLANK

REPORT DOCUMENTATION PAGE	*Form Approved OMB No. 0704-0188*

1. AGENCY USE ONLY *(Leave blank)*	**2. REPORT DATE** December 2022	**3. REPORT TYPE AND DATES COVERED** Master's thesis

4. TITLE AND SUBTITLE
GAN LIGHT EMISSION CONTROLLED DC-DC CONVERTER

5. FUNDING NUMBERS

6. AUTHOR(S) Justin D. Johnston

7. PERFORMING ORGANIZATION NAME(S) AND ADDRESS(ES)
Naval Postgraduate School
Monterey, CA 93943-5000

8. PERFORMING ORGANIZATION REPORT NUMBER

9. SPONSORING / MONITORING AGENCY NAME(S) AND ADDRESS(ES)
N/A

10. SPONSORING / MONITORING AGENCY REPORT NUMBER

11. SUPPLEMENTARY NOTES The views expressed in this thesis are those of the author and do not reflect the official policy or position of the Department of Defense or the U.S. Government.

12a. DISTRIBUTION / AVAILABILITY STATEMENT
Approved for public release. Distribution is unlimited.

12b. DISTRIBUTION CODE
A

13. ABSTRACT (maximum 200 words)

This work demonstrates the very first implementation of electroluminescence from a gallium nitride vertical diode as a feedback mechanism for real-time current control of a power converter. Current estimation via electroluminescence provides a galvanically isolated sensor capability that is not susceptible to electromagnetic interference, which is inherently produced in switch mode power supplies. The light feedback is converted to an electrical signal that is further digitally filtered to construct a 3D current calibration surface. This surface converts duty cycle and light signal intensity into a real-time current estimation utilized as a feedback parameter in a buck converter control system. The accuracy of current estimation is shown to be within 5% of steady-state current over various load conditions. Transient-state response was also demonstrated for step changes in commanded current and voltage within the power converter. Methods of increasing accuracy and reducing current estimation delay time are discussed.

14. SUBJECT TERMS
gallium nitride, buck converter, GaN, Electroluminescence, wide bandgap, SiC, silicon carbide, SMPS

15. NUMBER OF PAGES
85

16. PRICE CODE

17. SECURITY CLASSIFICATION OF REPORT	**18. SECURITY CLASSIFICATION OF THIS PAGE**	**19. SECURITY CLASSIFICATION OF ABSTRACT**	**20. LIMITATION OF ABSTRACT**
Unclassified	Unclassified	Unclassified	UU

NSN 7540-01-280-5500

Standard Form 298 (Rev. 2-89)
Prescribed by ANSI Std. 239-18

THIS PAGE INTENTIONALLY LEFT BLANK

Approved for public release. Distribution is unlimited.

GAN LIGHT EMISSION CONTROLLED DC-DC CONVERTER

Justin D. Johnston
Lieutenant, United States Navy
BSEE, University of New Mexico, 2015

Submitted in partial fulfillment of the
requirements for the degree of

MASTER OF SCIENCE IN ELECTRICAL ENGINEERING

from the

NAVAL POSTGRADUATE SCHOOL
December 2022

Approved by: Todd R. Weatherford
Advisor

Keith Corzine
Co-Advisor

Matthew A. Porter
Second Reader

Douglas J. Fouts
Chair, Department of Electrical and Computer Engineering

THIS PAGE INTENTIONALLY LEFT BLANK

ABSTRACT

This work demonstrates the very first implementation of electroluminescence from a gallium nitride vertical diode as a feedback mechanism for real-time current control of a power converter. Current estimation via electroluminescence provides a galvanically isolated sensor capability that is not susceptible to electromagnetic interference, which is inherently produced in switch mode power supplies. The light feedback is converted to an electrical signal that is further digitally filtered to construct a 3D current calibration surface. This surface converts duty cycle and light signal intensity into a real-time current estimation utilized as a feedback parameter in a buck converter control system. The accuracy of current estimation is shown to be within 5% of steady-state current over various load conditions. Transient-state response was also demonstrated for step changes in commanded current and voltage within the power converter. Methods of increasing accuracy and reducing current estimation delay time are discussed.

THIS PAGE INTENTIONALLY LEFT BLANK

TABLE OF CONTENTS

LIST OF FIGURES

THIS PAGE INTENTIONALLY LEFT BLANK

LIST OF TABLES

THIS PAGE INTENTIONALLY LEFT BLANK

LIST OF ACRONYMS AND ABBREVIATIONS

Ω	ohm
µF	microfarad
µH	microhenry
3D	three dimensional
A	amps
ac	alternating current
ADC	analog to digital converter
CCM	continuous conduction mode
cm	centimeter
cm^2	square centimeter
cm^3	cubic centimeter
D	duty cycle
DAC	digital to analog converter
dc	direct current
EL	electroluminescence
EMI	electromagnetic interference
eV	electronvolt
FOM	figure of merit
g	gram
GaAs	gallium arsenide
GaN	gallium nitride
IDE	integrated development environment
K	kelvin
kΩ	kilohm
LED	light emitting diode
m	meter
MHz	megahertz

MV	megavolt
N	negative doped
NPS	Naval Postgraduate School
nm	nanometer
P	positive doped
PI	proportional-integral
PN	positive doped-negative doped
PWM	pulse-width modulation
s	second
Si	silicon
SiC	silicon carbide
SMPS	switch mode power supplies
V	volt
W	watt

ACKNOWLEDGMENTS

I want to thank Matt Porter, Professor Weatherford, and Professor Corzine for the opportunity and support during this project. Shawn and Christina, thank you for being a sounding board for me during our educational journey. Lastly, I'd like to thank my wife Kira and kids Ashlyn, Rory, and Lorcus for putting up with my endless hours in the garage.

THIS PAGE INTENTIONALLY LEFT BLANK

I. INTRODUCTION

As the U.S. Navy strives to maintain its technological supremacy in an ever-increasingly competitive world, the need to adopt smaller, more efficient, and noise-resistant electronic solutions is paramount. Most modern shipboard technologies require a conversion of supplied electrical power from alternating current (ac) into a heavily regulated direct current (dc) for direct use or additional conversion back into ac for frequency manipulation or equipment voltage requirements. Due to the power conversion requirements, dc–dc converters are being designed to replace much larger, heavier, and low-frequency transformers for shipboard use. Maximizing the efficiency and space-saving benefits of dc–dc converters require high-frequency switching of electronic devices, which can introduce interfering noise into its control system via its inherent sensors or neighboring electrical systems. Finding a means to reduce the impact of self-generated and externally-generated noise to the shipboard dc–dc converters greatly improves the stability and controllability of power electronics equipment in shipboard operating environments.

Inductor current and output voltage measurements are desired for optimal dc–dc converter control. The efficiency required of modern dc–dc converters precludes the use of shunt resistors for current detection, as well as the nonlinear operation near saturation and bandwidth limitations of current transformers. This makes Hall effect sensors the ideal choice for shipboard dc–dc converters. Hall effect sensors measure current indirectly by sensing the current-generated magnetic field, similar to a current transformer. Due to the use of the Hall effect for B field sensing, the magnetic coupling between the wire carrying the sensed current and the Hall probe can be low, reducing the susceptibility of the sensor to external interference. However, Hall effect sensors come with their disadvantages. The high current operation of the measured circuit will cause increased inaccuracies due to temperature drift, and the potential for large offset voltages due to parasitic resistance requires additional circuitry to calibrate and obtain high accuracy measurements. Additionally, since the principle underlying the Hall effect is still based upon magnetic field coupling, stray inductive coupling from the dc–dc converter inductor introduces a non-negligible amount of noise into the current measurement, which can be compounded

by external electromagnetic interference (EMI) and the already present switch frequency noise. Furthermore, magnetic non-linearities contribute to the sensor noise.

A non-contact optically isolated solution would be ideal for providing similar advantages as the Hall effect sensor, while not being susceptible to EMI. Such a solution could be implemented by a sensor that generates an optical signal directly driven by the current to be measured. The use of established optoelectronic devices, such as LEDs in series with the measured current path, can be used to create an optical signal that is a function of the current. However, the addition of such devices adds additional loss and reactance to the switching converter, decreasing converter efficiency, and complicates control of the circuit. A better solution would be to sample luminescence generated directly from the semiconductor power switches, which are intrinsic to the operation of the converter; although traditional silicon (Si) power devices do not produce significant electroluminescence during operation. In contrast, high-power bipolar power switches made from direct band gap materials such as gallium arsenide (GaAs) and gallium nitride (GaN) will luminesce significantly during forward bias operation. Past work at NPS has demonstrated that electroluminescence from GaN power devices can be related to the instantaneous current and temperature of the device. With the emergence of vertical GaN bipolar power diodes, it has become a realistic possibility to directly implement switching converter control via the detection of luminescence signals from the power device.

A. RESEARCH OBJECTIVE

The purpose of this thesis is to explore the viability of utilizing experimentally derived relationships between light emission intensity and junction temperature of a GaN diode to demonstrate direct control of the output of a dc–dc converter circuit current via optically estimated current through the diode. The relationship between the luminescence, junction temperature, and forward current amplitude of a commercial GaN power diode is explored to determine application viability. To demonstrate current-based control, a buck converter is designed and constructed. Once an optimal method of obtaining a real-time current measurement has been established, it is used as a feedback input into the dc–dc converter control system to determine estimated current for system control.

B. RELATED WORK

The value of GaN semiconductors in power and microwave systems is becoming more evident to the military with its recent inclusion in the Navy SPY-6 [1] and the Army Q-53 radar [2]. As the manufacturing and prevalence of GaN increases, the exploration of the unique properties of GaN also increases. Beyond the advantages GaN represents in traditional use in power electronics it also belongs to a family of semiconductors that are direct band gap. This allows GaN bipolar devices to produce electroluminescence at a high efficiency as current passes through the device which led to the creation of the GaN-based blue-violet light emitting diode (LED) in the early 1970s. Other wide band gap materials including GaN have been investigated for utilizing emitted light to determine system parameters of the circuit they are embedded in. For example, Kalker investigated extracting current and temperature information from silicon carbide MOSFET body diodes using pattern recognition algorithms and neutral networks [3]. Additionally, Chengmin investigated extracting junction temperature from a silicon carbide (SiC) MOSFET body diodes used in a power inverter with a photosensitive circuit [4].

Past work at NPS has directly explored the relationship between current and electroluminescence in bipolar GaN power devices. Broeg explored the possibility of current estimation via electroluminescence from GaN positive doped-negative doped (PN) Junctions with optical filtering techniques [5]. The split filter technique was further investigated by Robinson, who compared the SiC MOSFET body diode and GaN power diode electroluminescence [6]. Williams expanded on the optical filtering method developed by Broeg to utilize the electroluminescence (EL) of a GaN diode for real-time current estimation of current using multiple photodiodes to build intensity contours to eliminate temperature as a requirement to directly extract current information as a feedback parameter [7].

C. THESIS ORGANIZATION

The design and control of buck converters, the electrical properties of WBG materials, the material and electrical properties of GaN, and commercially available current sensors are reviewed in Chapter II. An overview of the tested device, experimental setup,

and instrumentation are provided in Chapter III. Chapter IV summarizes the data collection and discusses experimental findings and results. Lastly, Chapter V provides an overview of the research performed and addresses recommended alterations and future research in this subject.

II. BACKGROUND

This chapter discusses the buck dc–dc converter topology, design, parameter measurement methods, and control. Additionally, it discusses the properties of wideband gap semiconductors and specifically the useful properties of GaN that make it an ideal choice for power electronics. The mechanisms of light emission from GaN are discussed as well as the calibration method for current sensing from GaN device EL.

A. SWITCH MODE POWER SUPPLIES

Modern civilian and shipboard electronic systems require a well-regulated and stable power supply that can perform well over a wide array of environmental and load conditions. Traditionally, this has been achieved by rectifying and filtering the output of large low-frequency transformers to meet the specific power requirements of the individual system. Switch mode power supplies are increasingly replacing the older line-frequency systems due to their compact size, reduced weight, and efficiency above 95%. Common switch mode power supplies (SMPS) include non-isolated dc–dc converters, forward converters, and flyback converters, the latter of which include a transformer for galvanic isolation. The most common dc–dc converter circuits are the boost, buck, and buck/boost. For this discussion we will focus on buck converters.

B. BUCK CONVERTER TOPOLOGY

There are two common topological layouts for buck converter circuits. These include synchronous and asynchronous buck converter layouts. Figure 1 shows a simplified circuit diagram for the synchronous configuration. This circuit utilizes two switches that are alternately driven by a gate drive circuit. The inductor and capacitor in this circuit form a low pass filter which removes the high-frequency switch noise from the output and allows the circuit to provide a continuous dc waveform.

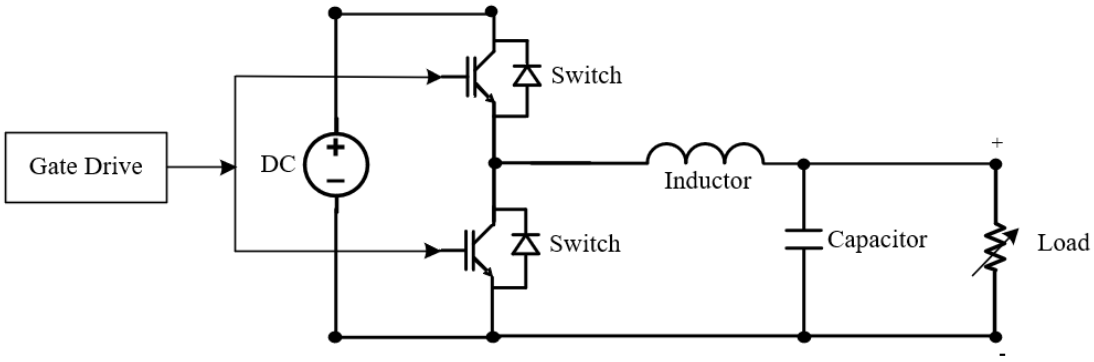

Figure 1. Synchronous Buck Converter Circuit. Adapted from [8].

Figure 2 shows a simplified circuit diagram of an asynchronous buck converter. The purpose of the freewheeling diode is to provide a current path when the switch is opened. This serves as an uncontrolled switch that operates in a similar way as the bottom switch of the synchronous configuration. The operation of the synchronous buck converter is the same except the freewheeling diode is replaced by another switch that allows additional control of the system. For the background discussion of this work, the focus will be on the asynchronous configuration which is what is used to implement optical current control via the EL emissions of the diode.

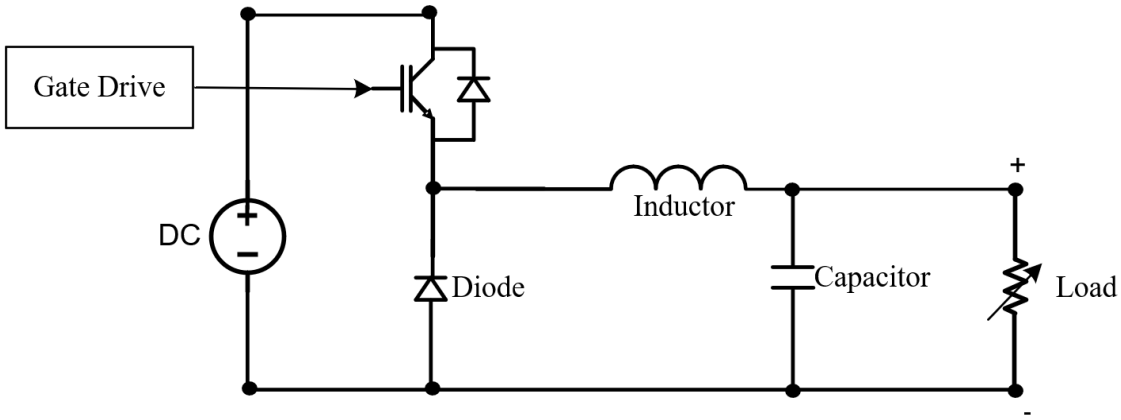

Figure 2. Asynchronous Buck Converter Circuit. Adapted from [9].

C. STEADY STATE BUCK CONVERTER OPERATION

The buck converter circuit in steady state switches between two different circuit configurations: on-state and off-state. During the on-state, current flows from the dc source to the load through the inductor, charging the capacitor, and building an electromagnetic field in the inductor. Since current cannot change instantly across the inductor and voltage across the capacitor as shown by (1) and (2), the output voltage is less than the input voltage. This current flow path is illustrated in Figure 3.

$$I = C\frac{dv}{dt} \tag{1}$$

$$V = L\frac{di}{dt} \tag{2}$$

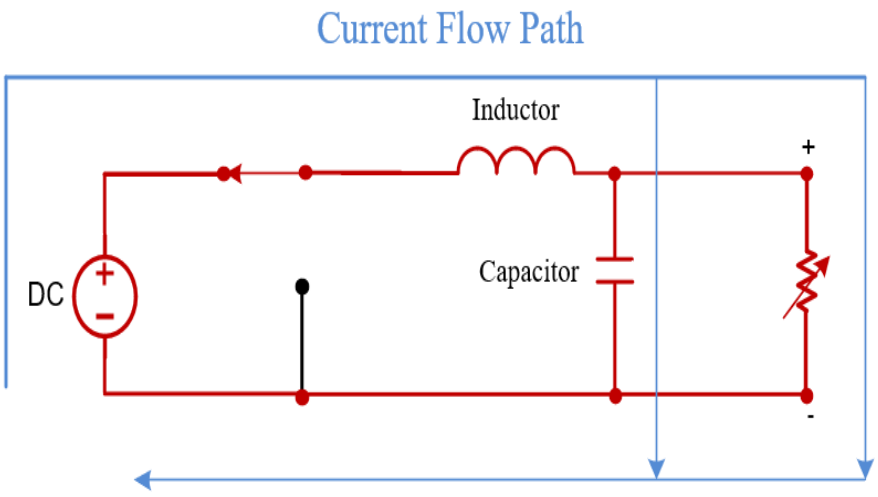

Figure 3. On-State Current Flow Path. Adapted from [10].

The off-state disconnects the dc source from the inductor, shorting the left node to ground. Since the inductor current cannot change instantly, a voltage is developed across the inductor. This resulting voltage charges the capacitor which supplies the output voltage to the load. The off-state current flow path is illustrated in Figure 4. The on-times for each

state are determined by the duty cycle and occur inversely proportional to the switching frequency.

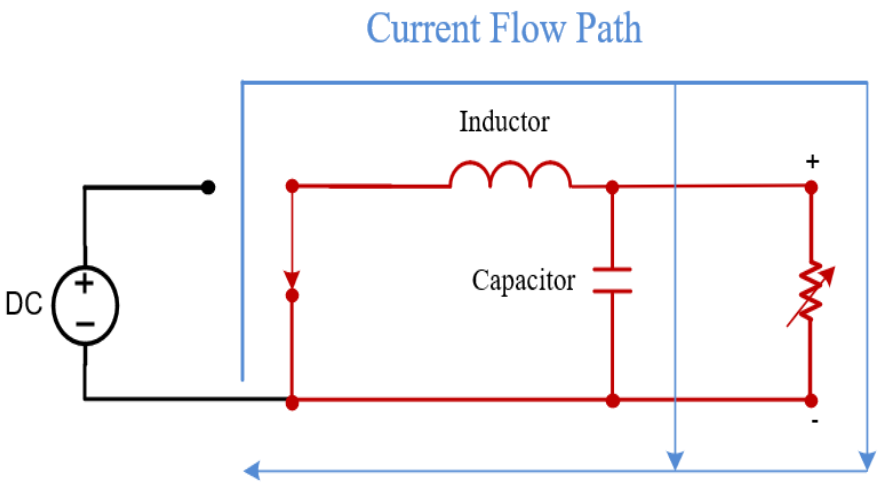

Figure 4. Off-State Current Flow Path. Adapted from [10].

Buck converters operate by reducing the output dc voltage below that of the input dc voltage which is common due to the large mains voltage present in ac electrical distribution systems. The reduced size and weight over inductive transformers are achieved by having large switching frequency (f_s).

$$L = \frac{(1-D)V_o}{\Delta I_L f_s} \tag{3}$$

$$C = \frac{(1-D)}{8L}\frac{V_o}{\Delta V_o}\frac{1}{f_s^2} \tag{4}$$

The desired ripple in both current and voltage is a design parameter taken into consideration prior to construction. Therefore, for given ΔI_L and ΔV_o design points in continuous conduction mode, as switching frequency is increased, the required inductance and capacitance are reduced as shown by (3) and (4) [11]. Figure 5 shows the ideal current

and voltage waveforms associated with a buck converter while in steady state in continuous conduction mode (CCM). CCM refers to the inductor current not crossing nor reaching zero during the off-state in a given period. If the inductor current of a buck converter does reach zero during the off-state, the buck converter is said to be operating in discontinuous conduction mode. The research of this paper will focus on buck converter operations while in CCM.

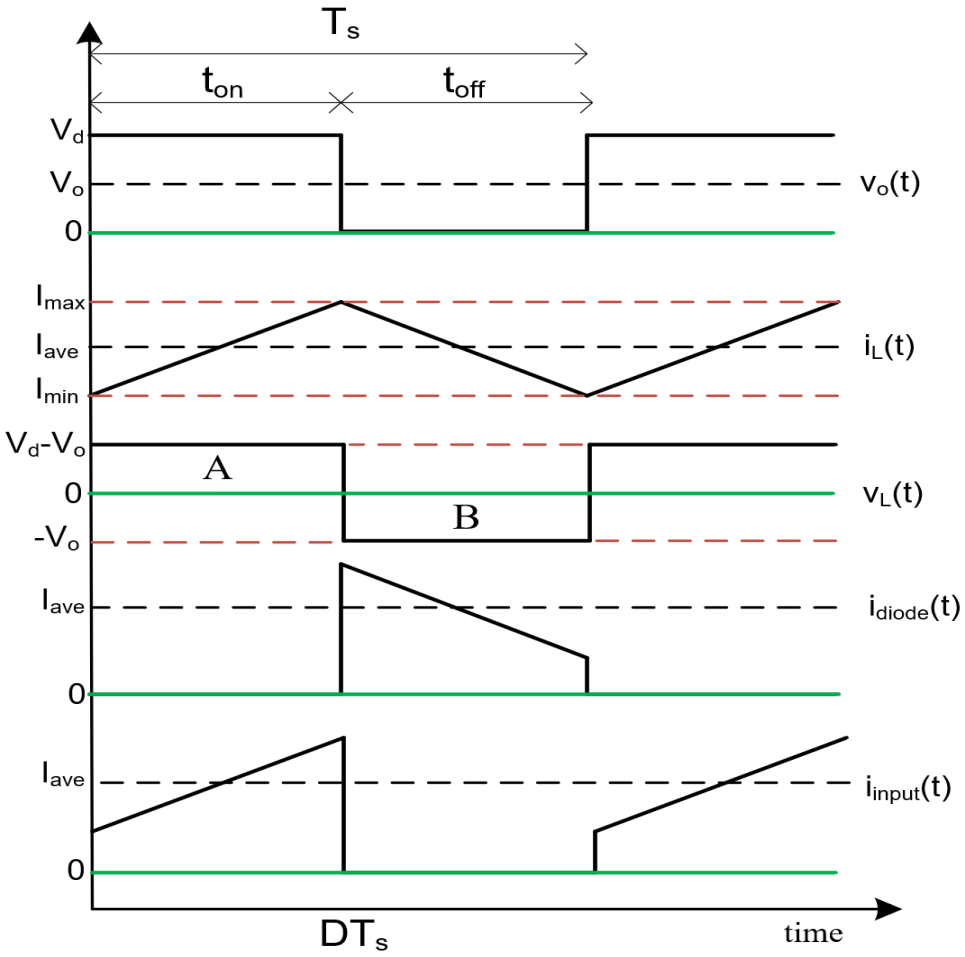

Figure 5. Ideal Buck Converter Waveforms. Adapted from [11].

The repeating waveform nature in steady state ensures that the integral of voltage in one period across the inductor equals zero per (5) [11].

$$\int_0^{T_s} v_L dt = \int_0^{t_{on}} v_L dt + \int_{t_{on}}^{T_s} v_L dt = 0 \tag{5}$$

Since voltage is proportional to current, this implies that the area A and B of the inductor voltage must be equal in Figure 5 [11]. Using these relationships, we can derive the duty cycle ratio as shown in (6).

$$\frac{V_o}{V_d} = \frac{t_{on}}{T_s} = D \tag{6}$$

From (6), it can be shown that the output voltage is a product of the duty cycle ratio and input voltage as shown by (7).

$$V_o = DV_d \tag{7}$$

Figure 5 further shows that inductor current is an amalgamation of the input current and diode current from on-state to off-state due to the potential difference across the inductor.

D. BUCK CONVERTER CONTROL

There are two largely used control methods for buck converters. The simpler of the two is voltage control as shown in Figure 6. In this control scheme, the output voltage alone forms the feedback loop and is compared to an external reference voltage. The error between the reference voltage and measured output voltage is fed through a proportional-integral (PI) controller that adjusts the pulse-width modulation (PWM) duty cycle to reduce that error to zero.

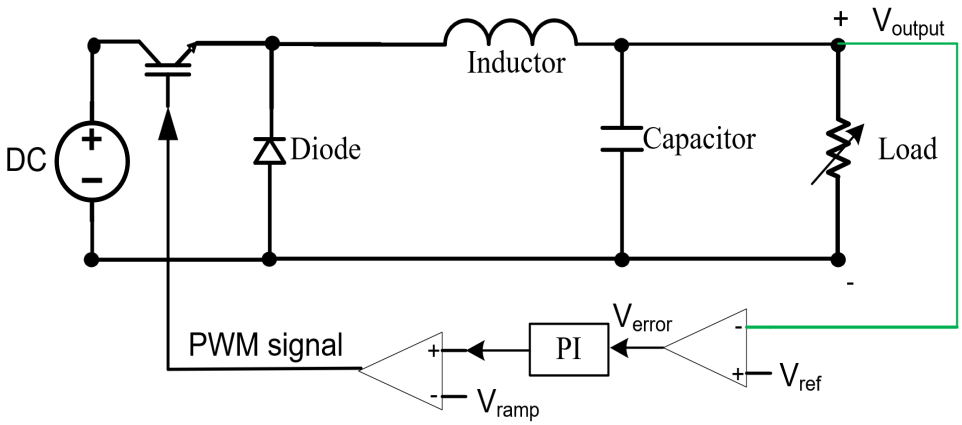

Figure 6. Simplified Voltage Mode Buck Converter. Adapted from [12].

This method does not provide inherent overcurrent protection since current is not measured during operation. This method also has a slower settling time since the change in load must be detected as a change in output voltage before an error signal can be generated [13]. The second method is current control as shown in Figure 7. This method increases the complexity of the control circuitry since it adds a second control loop that utilizes the current of the inductive element along with output voltage.

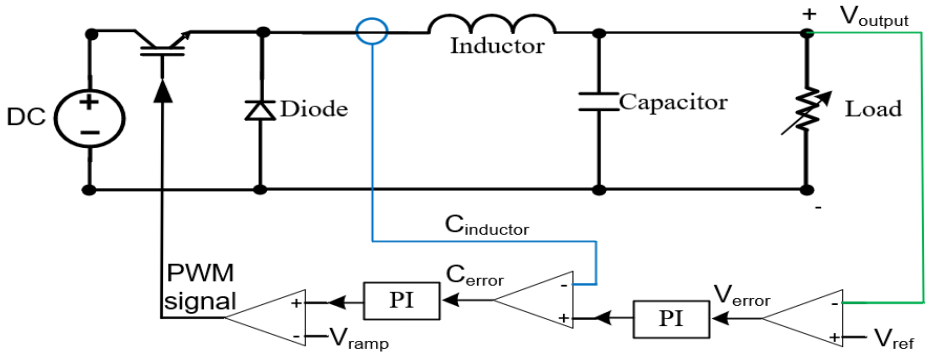

Figure 7. Simplified Current Mode Buck Converter. Adapted from [14].

The output of the above-mentioned PI controller is compared to the measured current, and this error is fed into a second PI controller which reduces the overall system error to zero in the same manner as the voltage control method. This control method has

inherent overcurrent protection and faster response times due to inductor current slope and magnitude changes due to the difference in input-to-output voltage [13]. This provides faster line-to-load changes than voltage mode control [13]. The controls differ based on the method the current is measured and analyzed. For example, there are control schemes that utilize peak, average, and valley inductor currents for feedback. Peak current control has poor noise immunity, and valley current mode has poor line regulation. Average current mode control has excellent noise impunity and can be used in any current branch which makes it ideal for this research [15].

E. HALL EFFECT CURRENT SENSING

There are several ways to measure circuit current for converter control. Traditional methods use resistive or magnetic elements and include current transformers, shunt resistors, fluxgate transformers, and Hall effect sensors. Hall effect sensors are the most popular since they do not introduce significant inductance or resistance, operate at high frequencies, and can be employed in a wide array of environments. Hall effect sensors work by measuring the magnetic field of a conductor near the sensor. A small proportional output voltage is generated in the sensor that then must be corrected for temperature and offset, then amplified with additional circuitry [16], [17]. Since the sensor measures local magnetic fields, this makes the Hall effect sensor susceptible to EMI. Figure 8 shows a simplified Hall effect sensor circuit.

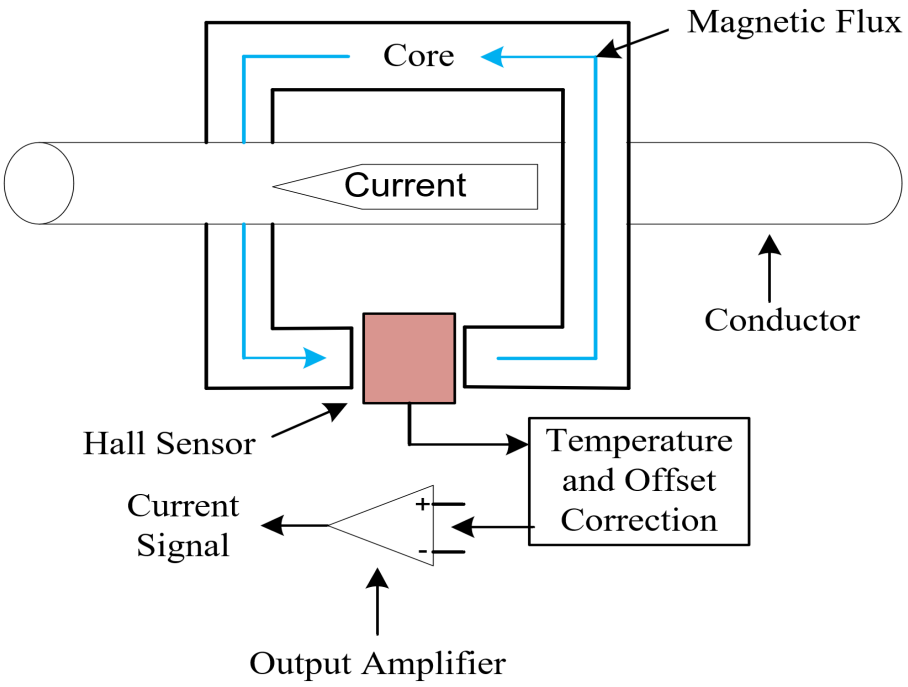

Figure 8. Simplified Hall Effect Sensor. Adapted from [17] .

A disadvantage of Hall effect sensors is their susceptibility to external EMI [18]. Sensor orientation and proximity to electromagnetic fields directly affect the EMI intensity. Figure 9 shows the EMI noise spectrum as a function of current. High switch frequency SMPS produce substantial EMI due to the hard switching nature of their operation. Since SMPS utilize Hall effect sensors to measure feedback parameters for control, this added EMI can introduce instability into their operation.

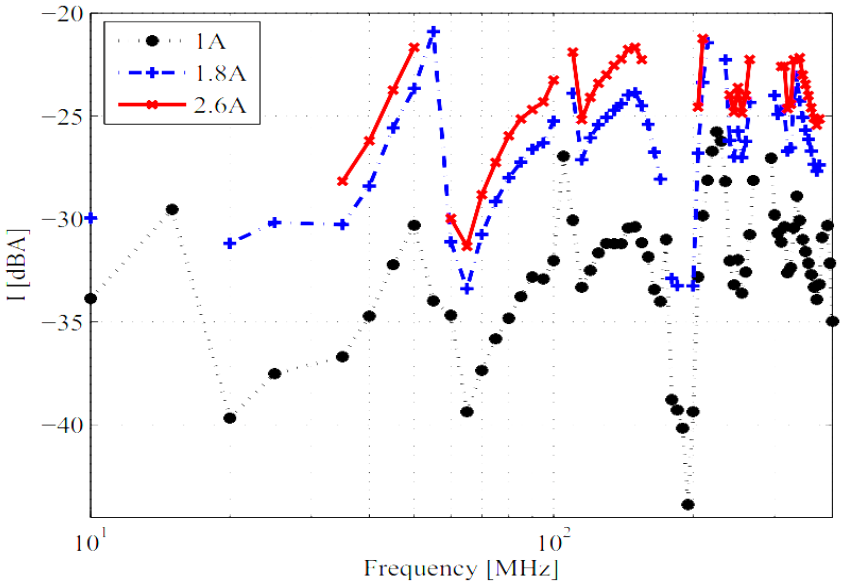

Figure 9. Measured Bulk Current Injection Immunity Level of Hall Effect Sensor at Varied DC Currents. Source: [18].

F. GAN PN DIODE PROPERTIES

1. Electronic and Material Properties of GAN

Silicon devices have dominated the electronics market for the last seven decades. With the need for decreased size and increased efficiency for modern power electronic applications, new semiconductor materials are becoming more readily available. WBG semiconductors are characterized by having a band gap higher than 2.2 eV, whereas silicon has a band gap of 1.12 eV. GaN meets this requirement with a band gap energy of 3.44 eV [19]. GaN is a direct band gap material [20] that allows an electron to move from the conduction band to the valence band with a photonic emission alone rather than a phonon and photon as with Si. The mechanisms of light emission in direct band gap materials such as GaN will be discussed in more depth in the next section. GaN has additional material properties that aid in its use in modern power electronics. The critical electric field at breakdown of GaN is an order of magnitude greater than Si at 3.3 MV/cm and 33.33% higher electron mobility which is tightly correlated to Baliga's Figure of Merit (FOM) [21] which is discussed in detail in the next section. GaN and Si have roughly the same thermal conductivity. A side-by-side comparison is shown in Table 1.

Table 1. Si vs. GaN Semiconductor Materials. Adapted from [19], [22].

Semiconductor Material	Si	GaN
Band gap (eV)	1.12	3.44
Direct or Indirect Band gap	Indirect	Direct
Electron Mobility ($cm^2/V•s$)	1500	2000
Density (g/cm^3)	2.33	6.1
Critical of Breakdown Field (MV/cm)	0.3	3.3
Thermal Conductivity (W/ m•K)	130	110

2. GAN PN Diode Structure

A PN diode is constructed of the junction of a P-type and N-type semiconductor material. At the bonding site, a depletion region is created due to electrons diffusing across the junction from the N-type material and recombining with holes in the P-type material. The opposite is also true with holes diffusing across the junction from the P-type material side and recombining with electrons in the N-type material side. Due to the heavy doping of the P-type material of the GaN diode, we assume the depletion width on the P-side is negligible [23]. With this assumption, we can analyze the GaN PN diode as having an ideal drift region due the large doping concentration on the P-side, small doping concentration on the N-side, and uniformly doped drift region [21]. This results in a triangular electric

field distribution with the peak electric field at the junction and the lowest electric field at the maximum depletion width, as shown in Figure 10 [21].

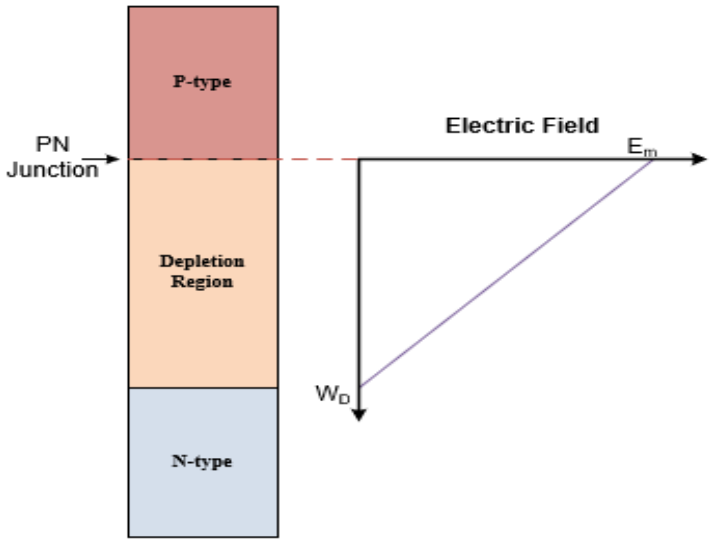

Figure 10. Ideal Drift Region of GaN Diode with High P-Side Doping and Associated Electric Field Distribution. Adapted from [21], [23].

The specific on-resistance ($R_{on.sp}$) of an ideal drift region is shown in Equation 8 which is a function of the width of the drift region (W_D), the doping of the material (N_D), mobility of the material used (μ_n), and charge of an electron (q) [21].

$$R_{on.sp} = \frac{W_D}{q\mu_n N_D} \tag{8}$$

Equation (8) can be modified by redefining depletion width and doping concentration in (9) and (10). The depletion width under breakdown condition can be defined as a function of desired breakdown voltage (BV) and critical electric field of the semiconductor material (E_C) [21]. The doping concentration (N_D) of the drift layer

required for the desired breakdown voltage can also be related to the critical electric field, dielectric constant (ε_s), electron charge, and breakdown voltage [21].

$$W_D = \frac{2BV}{E_C} \tag{9}$$

$$N_D = \frac{\varepsilon_S E_C^2}{2qBV} \tag{10}$$

We can combine the above equations, eliminating geometry-dependent terms, to give the ideal specific resistance in terms of Baliga's FOM, which is $\varepsilon_S \mu_n E_C^3$ as shown in the denominator of Equation 11 [21].

$$R_{on-ideal} = \frac{4BV^2}{\varepsilon_S \mu_n E_C^3} \tag{11}$$

Baliga's FOM is purely material dependent and indicates the tradeoff between optimal drift region on-state resistance and breakdown voltage. Figure 11 and Equation 11 show how GaN high critical electric field and high mobility result in a lower drift resistance than Si or SiC for a given breakdown voltage for a drift layer.

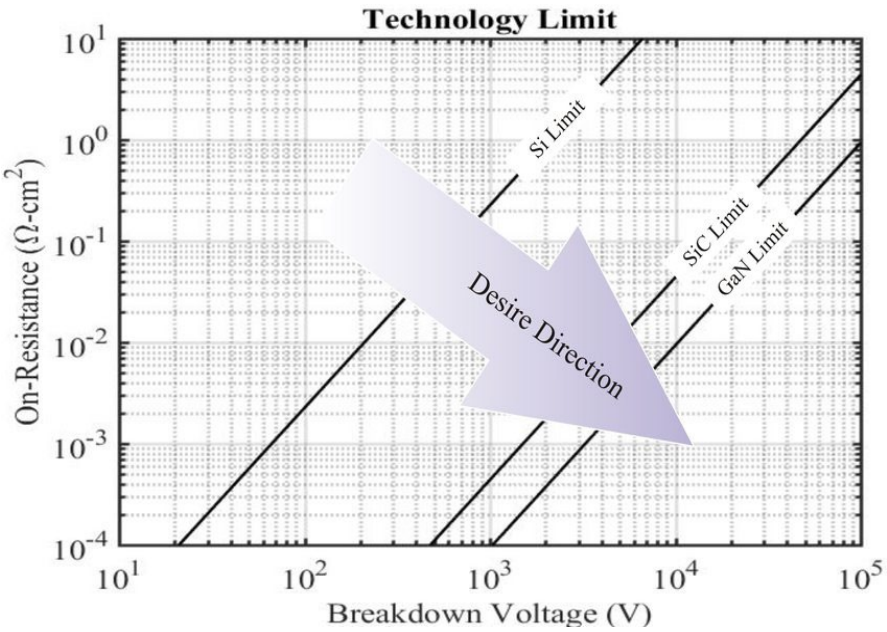

Figure 11. On-state Resistance vs. Breakdown Voltage of Semiconductor Materials. Source: [24].

3. PN Losses and Reverse Recovery Time

The lower on-state resistance of a GaN PN diode indirectly improves reverse recovery time as shown by Figure 12. The negative slope between t_1 and t_2 is increased, effectively reducing the Δt due to the smaller physical die area which eliminates the effects of inductance external of the diode [21]. The direct band gap of GaN allows faster recombination to remove excessive charge between t_2 and t_4. These effects allow the reverse recovery time of GaN PN diodes to be measured in nanoseconds, whereas silicon is in milliseconds. These effects allow the operation of GaN PN diodes at higher switch frequencies which allows for reduction in reactive element size in power converters.

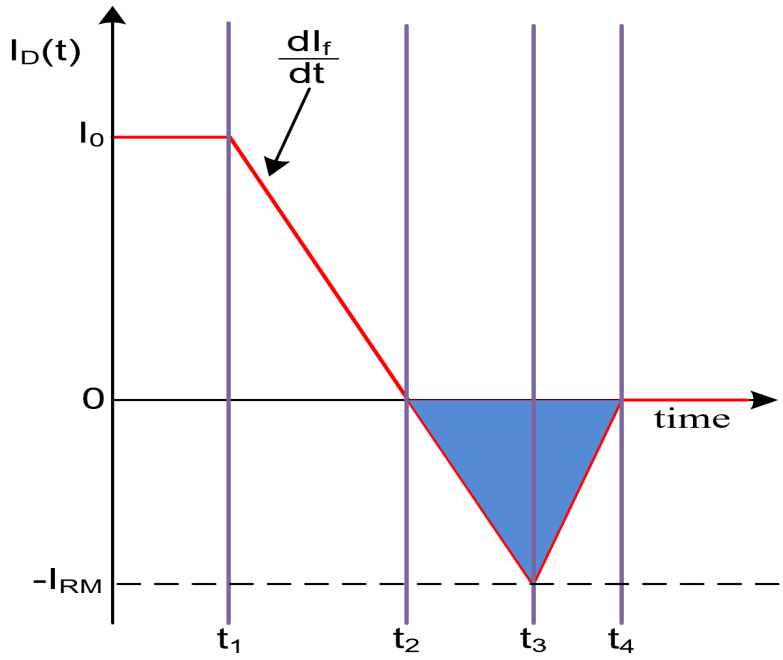

Figure 12. Diode Current During Reverse Recovery. Adapted from [25].

Power losses in a power diode can be broken down into conduction losses and switching losses. Total power losses in the diode are shown in (13). Baliga's FOM shows that the on-state resistance is low for the GaN diode which reduces the conduction losses. The reduced area size of the die lowers the parasitic capacitance, and the faster reverse recovery time reduces the switching losses. Equations (12) and (13) show the dependence of device power loss on the on-state resistance, reverse recovery time, device capacitance, and switching frequency. Faster recovery times and reduced power losses make GaN an ideal material for high-power SMPS.

$$t_b = t_4 - t_2 \tag{12}$$

$$P_D = (I_{on}^2 R_d + V_F I_{on})(1-D) + \frac{1}{2} C_d V_d^2 f_{sw} + \frac{1}{6} I_{RR} V_d t_b f_{sw} \tag{13}$$

4. Electroluminescence of GAN PN Diodes

In a semiconductor material, recombination occurs when a conduction band electron recombines with a hole in the valence band. The energy of the electron-hole system is conserved before and after this process by emitting either a series of phonons or a photon as shown by Figure 13. Due to the indirect band gap of Si during band-to-band recombination, phonons, which are quasiparticles associated with the vibration of a crystal lattice structure, are primarily emitted. GaN is a direct band gap material that primarily emits a photon during recombination through two different mechanisms. A photon at the energy of the band gap is emitted in direct band-to-band recombination. In this process a free electron combines directly with the vacancy in the electron shell [26]. This differs from excitonic recombination in that it is immediate. Excitonic recombination involves the formation of a hydrogen-like state between an electron and a hole, called an exciton, before recombination. The formation energy of the exciton reduces the energy of the emitted photon in comparison to direct band-to-band recombination [26].

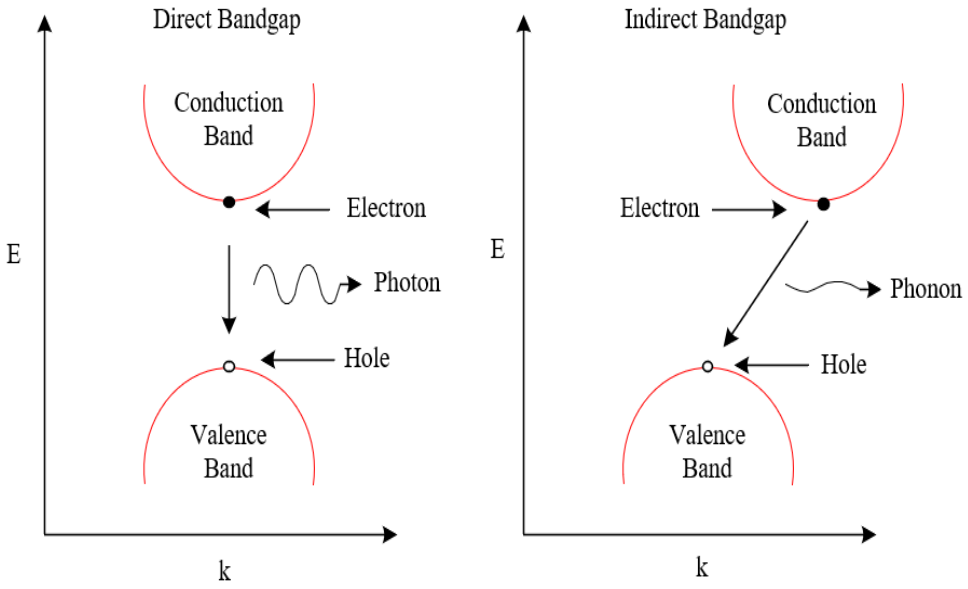

Figure 13. Direct vs. Indirect Band Gap. Adapted from [27], [28].

Forward biasing of the GaN PN junction increases the radiative output of the diode since the electrical current supplies additional holes and electrons to recombine. The EL spectra of GaN exhibit two peaks at roughly 390 nm due to excitonic emission and 570 nm caused by impurities in the fabrication process [5]. The EL out of a GaN diode is dependent on both current and temperature. Figure 14 shows a strong temperature dependence at the 390 nm peak and two intensity inversions prior to the 570 nm peak. Also, the EL peaks both slightly shift to the right as temperature and current are increased. Figure 15 shows a strong current dependence across the entire EL spectra.

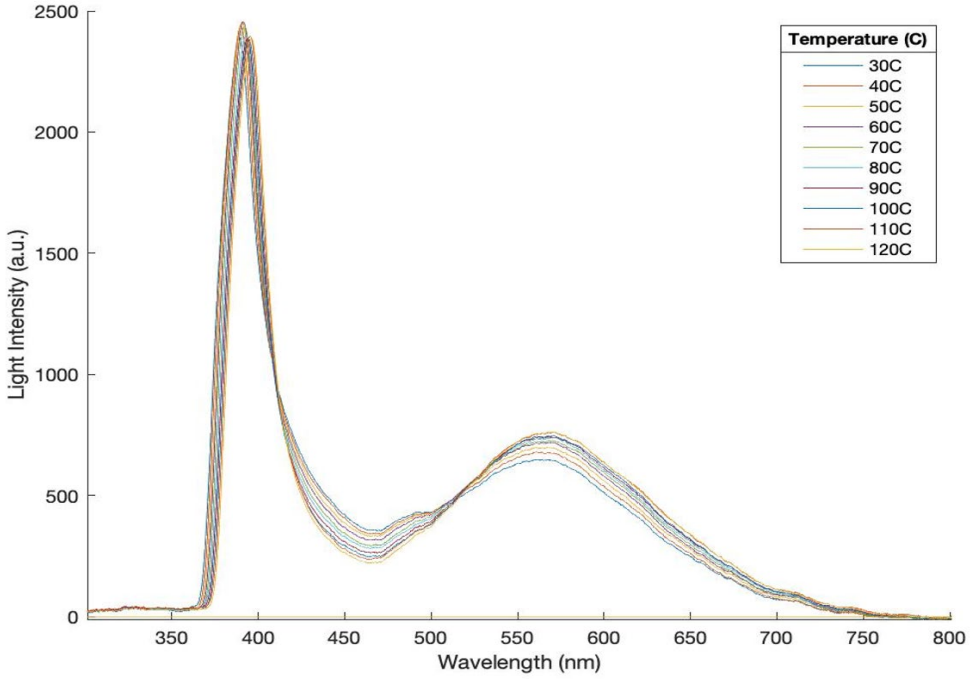

Figure 14. GaN Spectra at 1.0 A with Varying Temperature. Source: [29].

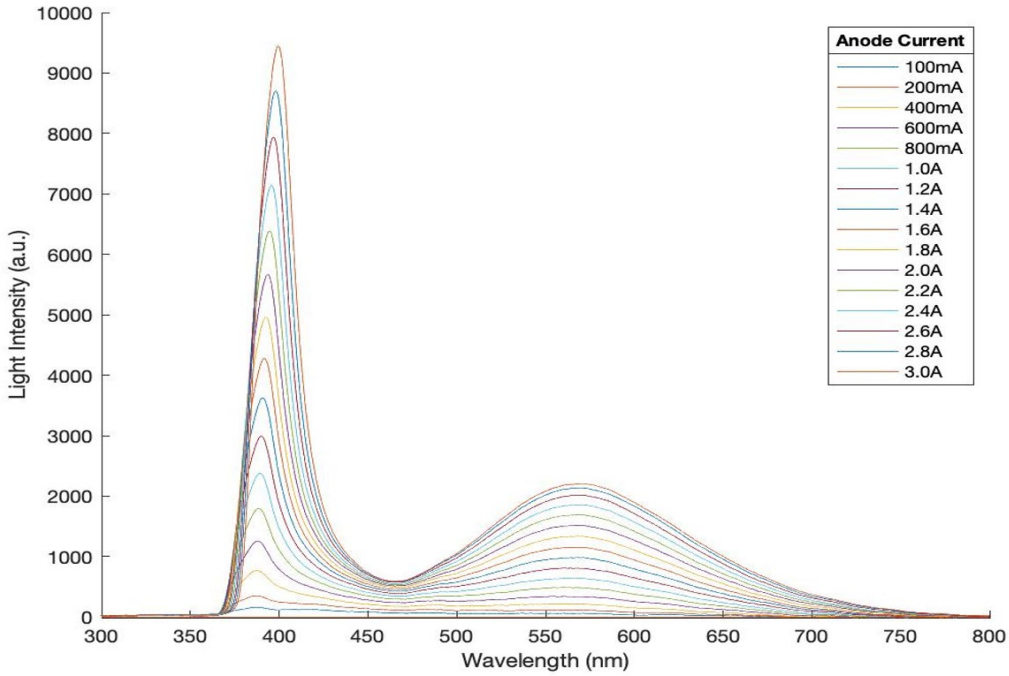

Figure 15. GaN Spectra at 30 °C with Varying Current. Source: [29].

Since both temperature and current affect the EL output, both temperature and EL intensity would need to be known to estimate the current in the GaN material. The difficulty is obtaining a real-time temperature at the GaN junction during operation.

5. Theory of Calibration

Broeg created an optical current calibration method by using a pulsed current source to generate fixed-duty cycle square waves with the GaN diode as a series load [5]. A singular 10 nm optical filter was centered at spectra peaks of interest and the EL was measured over varying current and temperature ranges to create multiple 3D surfaces to investigate the spectra range best suited for current estimation [5]. Williams tested a digital signal processor (DSP) based microcontroller implementation utilizing a lock-in amplifier detection method [7]. Porter et al. produced an experimental calibration method that utilized two optical filters at 390 nm and 420 nm [30]. EL measurements were recorded over varying current and temperature ranges to create two separate 3D surfaces that are represented by (14) and (15).

$$S1 = f1(I,T) \tag{14}$$

$$S2 = f2(I,T) \tag{15}$$

Using both optical sensor inputs simultaneously, the polynomial was solved using Newton's method to use the last solution as the initial guess for the next sensor acquisition. This resulted in high accuracy at steady conditions, but the iterative approach created long delays during transients. This approach was also limited due to temperature as a required input variable which is problematic to measure at the junction.

In (14) and (15) temperature is dependent on power loss in the GaN diode as shown by (16).

$$P_{loss} = P_{on}(1-D) + P_{sw} \tag{16}$$

This allows for the substitution of the duty cycle, which is a control variable easily calculated during operation, in the place of the unknown junction temperature which is difficult to obtain. Additionally, the 390 nm peak of the GaN spectra has the highest temperature dependence as shown previously in Figure 14. If an optical filter is employed to remove the heavily temperature-dependent section of the spectra, the variation in EL would more closely represent current regardless of thermal transients. Since the duty cycle is relatable to the output power of a current controlled buck converter, a 3D surface can be experimentally derived to relate the duty cycle and EL intensity to the diode current.

THIS PAGE INTENTIONALLY LEFT BLANK

III. EXPERIMENTAL DESIGN AND CALIBRATION

The following chapter will discuss the hardware and software selected for this experiment. To facilitate rapid prototyping, readily available commercial-off-the-shelf components were used. This proof of concept was designed to demonstrate the extraction of system current using electroluminescence from a GaN PN flyback diode and utilizes that quantity in the feedback loop of the buck converter control system in real time. The future work chapter will discuss improvements to this design to achieve faster transient response. Figure 16 is the overall system schematic and will be discussed in greater detail throughout this chapter. The elements of design can be broken down into three main modules as shown in Figure 17.

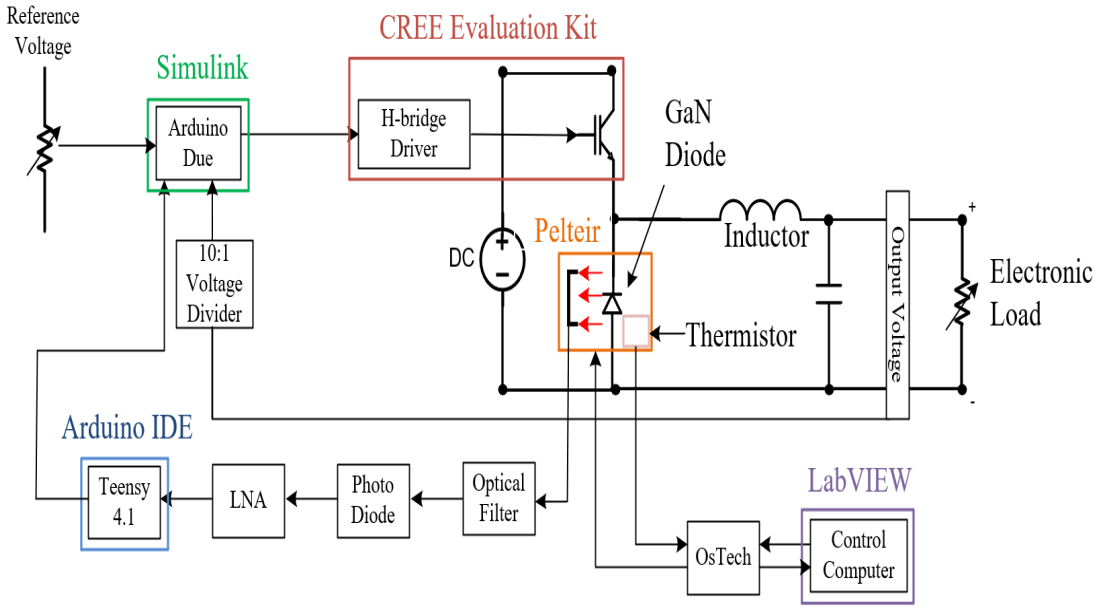

Figure 16. Overall System Schematic

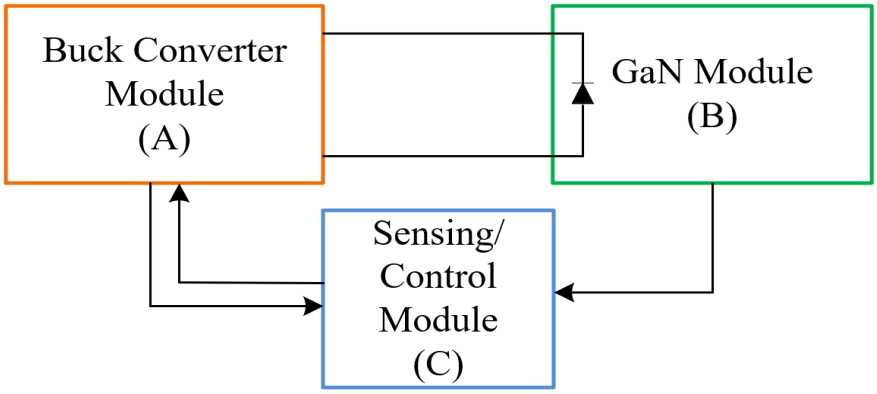

Figure 17. Simplified System Schematic

A. BUCK CONVERTER MODULE

Since the objective of this research is to determine the viability of extracting current information from GaN EL, output ripple, size, and efficiency of the buck converter were of little concern. A 100 kHz switch frequency was selected to ensure the design was representative of modern buck converters, yet within the microcontroller limitations discussed later in this chapter. To ensure maximum light emission during the off-state, the buck converter was designed to remain in CCM under all load conditions. To facilitate this and future work capacity, the capacitor and inductor were purposefully oversized to achieve this goal.

The gate drive and half bridge were comprised of a Wolfspeed KIT8020CRD8FF1217P-1 Silicon Carbide MOSFET evaluation kit. A depiction of this module is shown in Figure 18. The JM1 jumper was desoldered and lifted to split the half bridge. This allowed the GaN diode to replace the bottom MOSFET as shown by Figure 19.

Figure 18. KIT8020CRD8FF1217P-1 Wolfspeed SiC MOSFET Evaluation Kit. Source: [31]

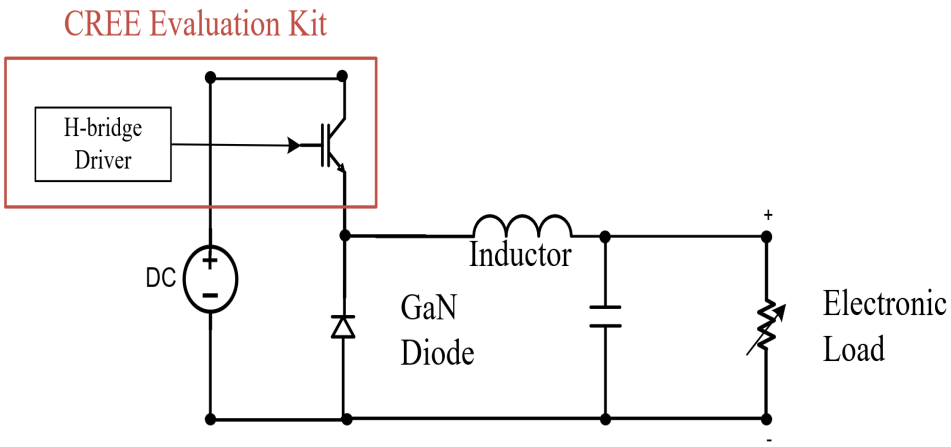

Figure 19. Buck Converter Circuit

The diode used was a commercially available vertical GaN PN diode in a TO-257 package shown in Figure 20. This diode batch was characterized by Broeg [5] and was found to have a forward voltage of 3.1 V, an on resistance of 0.2 Ω, and breakdown voltage of 1200 V. The implementation of the diode will be discussed in greater detail in the next section. The inductors are two series connected Dale IHC-30-150 for a total of 300 μH inductance. The low pass filter capacitor was constructed of 60 0.47 μF MKP-X2 capacitors in series for a total of 27.12 μF of capacitance and ESR of 0.33 Ω. A Tekpower TP3710A electronic load was used to provide variable load conditions and external voltage and current measurements.

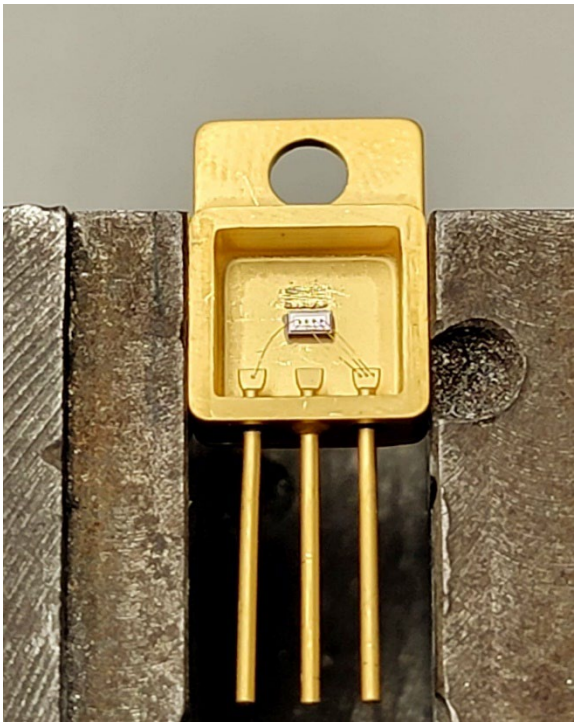

Figure 20. Unmodified TO-257 GaN Diode Package

B. GAN MODULE:

A similar method of optically coupling the GaN diode and fiber optic cable was employed as in previous work by Williams [7]. To maximize the EL capture, the TO-257 GaN diode package was modified with a jewelry saw as shown in Figure 21. This configuration allowed for centering of the linear slit SMA905 connector of the 1:4 Thorlabs multimode fiber bundle perpendicular to the light emission plane of the diode with a custom SMA holder on a J-bar mount as shown by Figure 22.

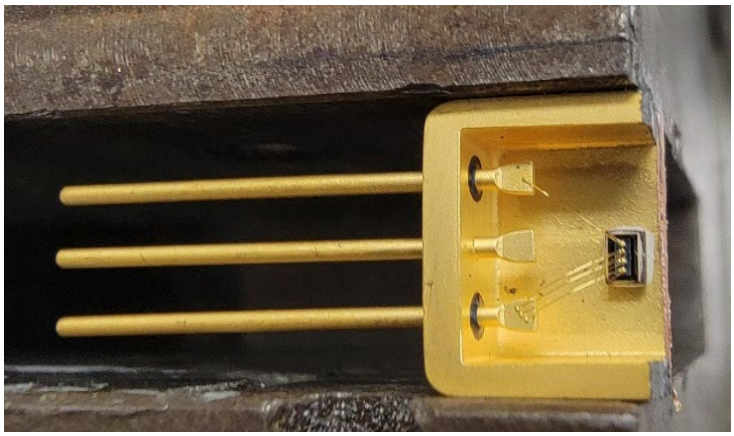

Figure 21. Modified GaN Diode Package

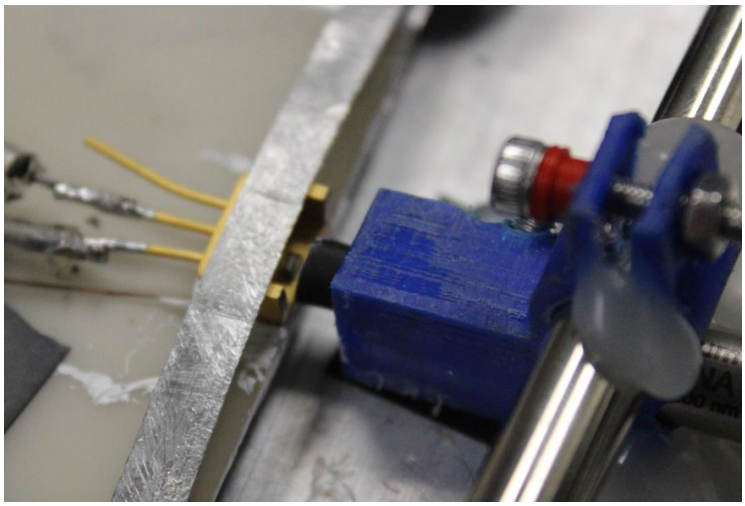

Figure 22. GaN Diode Butt Coupling

For active temperature control of the diode, two Peltier modules wired in series and controlled by a PS01-PA12v20 Ostech TEC controller were used. Temperature detection was accomplished with a 40 kΩ thermistor in direct contact with the modified TO-257 GaN diode package as shown in Figures 23 and 24. The Ostech interfaced with LabView on a standalone computer. An aluminum nitride wafer was utilized to electrically isolate the GaN diode from the heatsink to minimize EMI production shown in Figure 23.

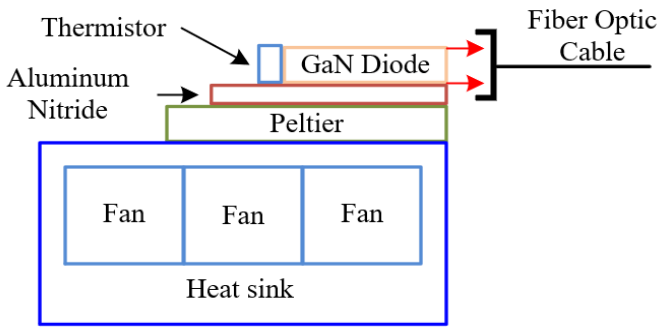

Figure 23. Mounted GaN Diode Module Configuration

Before its inclusion the switch noise produced from the electrically connected GaN heatsink during operation was significant enough to disrupt the operation of the Ostech temperature monitoring hardware through induction into the Peltier coolers. Several insulators were tested, but the electrical and thermal properties of aluminum nitride made it the superior choice.

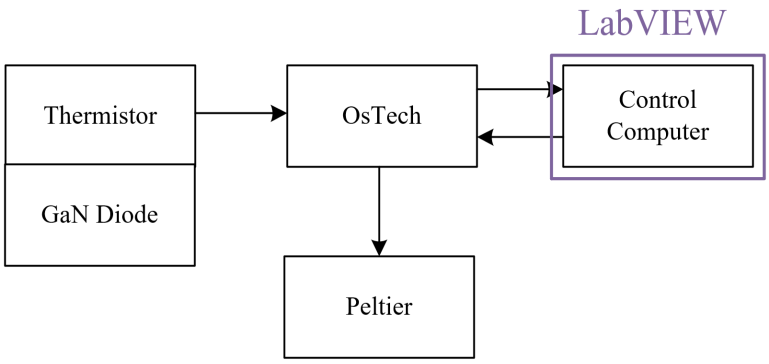

Figure 24. Temperature Monitoring and Control

Active temperature control was necessary to minimize the thermal capacitance that existed between the GaN diode and heatsink due to the thermal resistance of the aluminum nitride wafer. This reduces the thermal transients experienced during large duty cycle changes. The heat sink was sized to offer significant mass to ensure extended run times of the system with minimal forced air cooling.

C. SENSING AND CONTROL MODULE

The control and sensing module utilized two different programming suites to implement the controls and parameter measurements. The controls, voltage measurement, and post initial current sampling and filtering were implemented by Simulink which allows rapid prototyping in a graphical programming language. It also has the added advantage of directly exporting information to MATLAB for data acquisition and analysis. The initial current sampling and filtering was performed with the Arduino IDE. The Arduino IDE provides a large array of prebuilt open-source libraries for quick implementation and fine-tuning prototype designs.

1. Voltage Sensing

System efficiency was not a concern for this proof of concept which allowed the use of a 100 kΩ 10:1 voltage divider to be employed for output voltage measurement as shown by Figure 25. An 84 MHz Arduino Due as shown in Figure 26 which has one analog to digital converter (ADC) multiplexed across all analog input channels was used to sample the divided voltage signal.

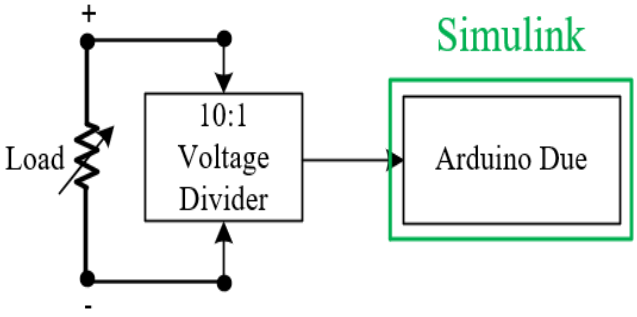

Figure 25. Voltage Detection

Figure 26. Arduino Due. Source: [32]

Once sampled, a digital averaging filter was used to remove the undesired high frequency components. The sample window of the averaging filter directly affects the delay imparted into the voltage feedback loop. To ensure acceptable voltage overshoot and quicker system response to voltage transients, a small filter window was used. Due to sampling error and the high EMI environment, the measured voltage at the buck converter output was not accurate. A Fluke 77 III and the electronic load was used to determine the voltage error from 20%–80% as shown in Figure 27. A MATLAB function block was used in Simulink to correct the error to less than 0.1 V by detecting the demanded duty cycle and subtracting the difference from the sampled voltage to ensure proper operation of the buck converter.

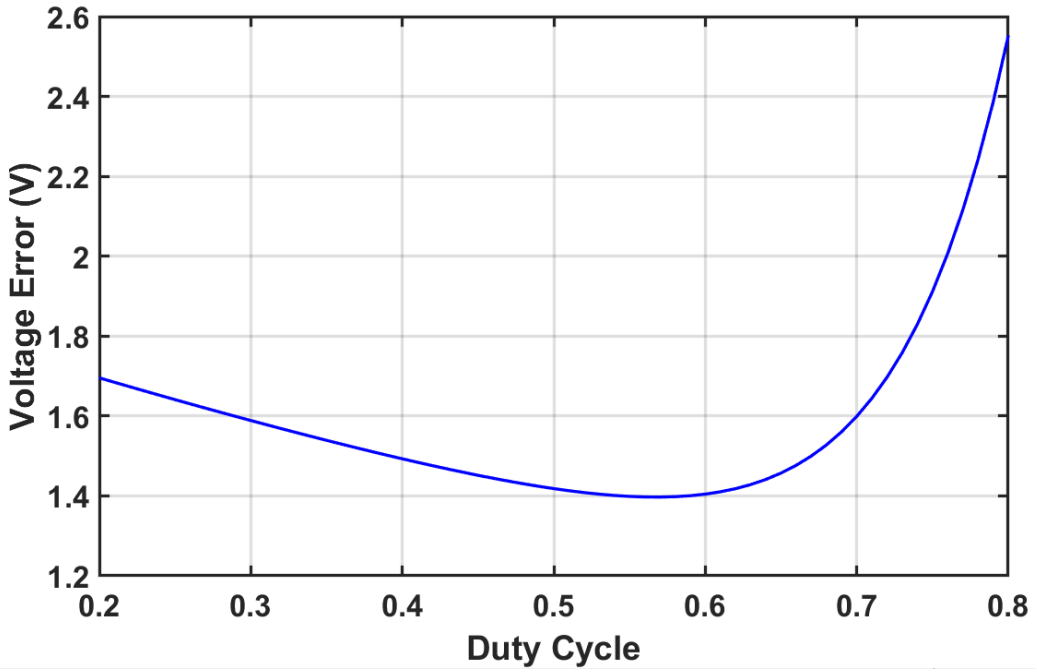

Figure 27. Voltage Error between Sampled Voltage and External Measured Voltage

2. Current Sensing

Figure 28 shows a block diagram of the high-level current detection method. The Arduino Due then resampled the digital to analog converter (DAC) output from the Teensy 4.1. Since the output electrical signal no longer contained the high frequency switch components, the Arduino Due could accurately sample with its hardware limitations. Additional filtering was performed to remove transmission noise and produce a constant output signal that could be measured during calibration.

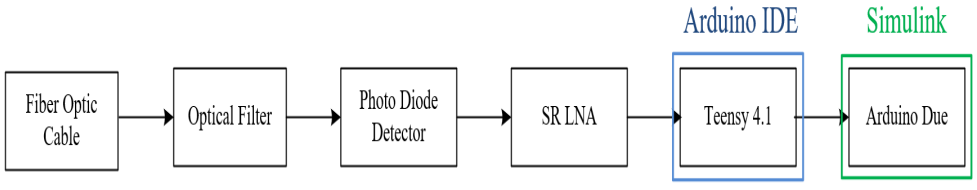

Figure 28. Current Detection and Sampling

The EL signal of the GaN diode is converted to an electrical signal via a ThorLabs APD130A2 photo detector after being optically filtered with a Thorlabs 450 nm high pass filter to reduce temperature dependance on the GaN EL spectra. A Stanford Research 560 low noise amplifier is then used to amplify and condition the signal for sampling. Due to the multiplexed ADC of the Arduino Due it proved to be inadequate to meet the minimum Nyquist sampling requirements.

Figure 29. Teensy 4.1. Source: [33]

A Teensy 4.1 microcontroller as shown by Figure 29 was overclocked to 816 MHz to provide dedicated sampling for the diode current signal. The sampled current signal was then filtered with a median and average filter onboard the Teensy 4.1 before being passed to the Arduino Due via an external DAC as shown by Figure 30.

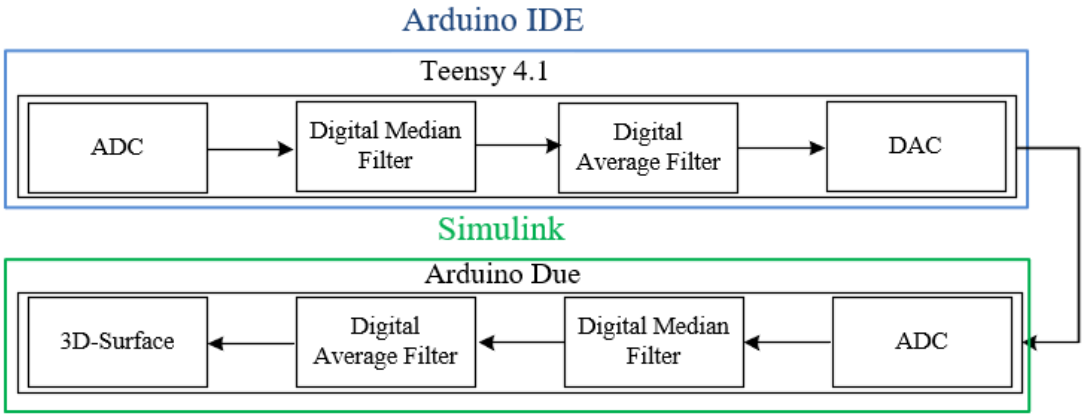

Figure 30. Expanded Teensy to Arduino Due Communication

Figure 31 shows diode current at the output of the ThorLabs photodiode prior to being sampled by the Teensy 4.1. The inductor current was externally measured by a

Tektronix TCPA300 AC/DC current probe and monitored on a Keysight DSOX1304t oscilloscope to ensure the buck converter was operating in CCM.

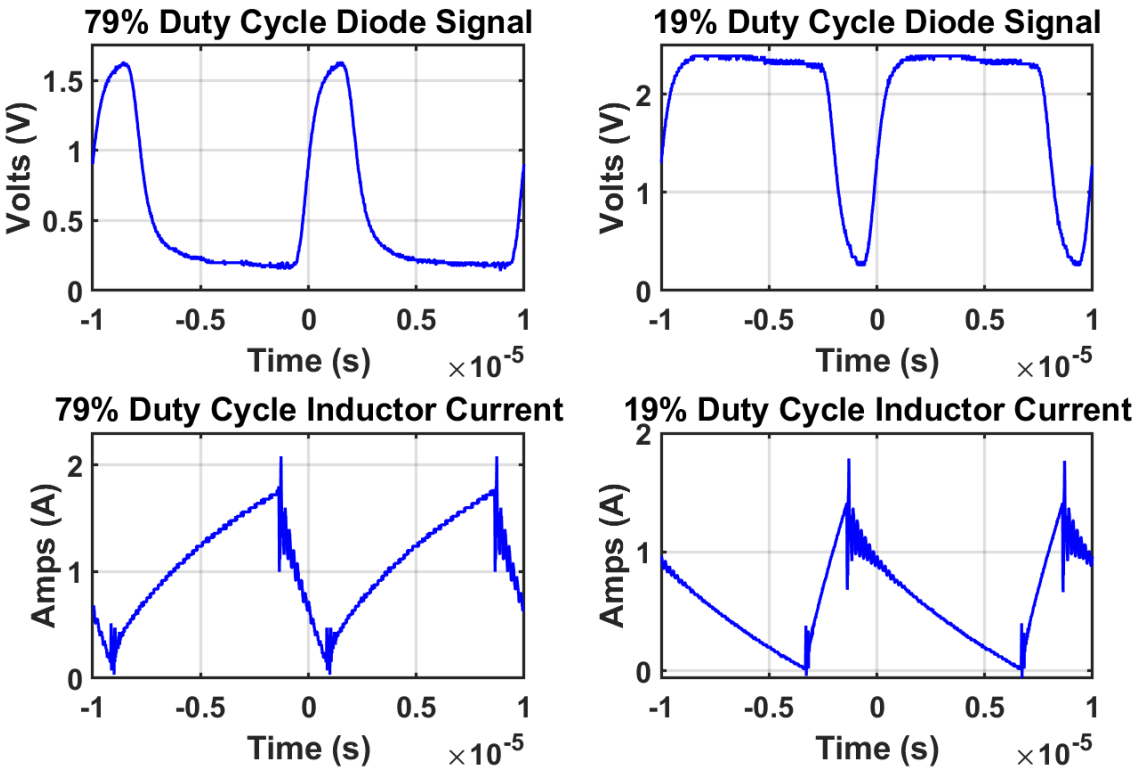

Figure 31. Oscilloscope Capture of 79% and 19% Duty Cycle Diode/Inductor Current Waveform

3. Calibration and Current Surface

As previously discussed, the 390 nm peak in the GaN EL spectrum is most affected by changes in junction temperature. The 390 nm peak also has the highest intensity value which means that the large change of that peak intensity drastically changes the magnitude of the output electrical signal. By filtering the section of the spectrum most affected by temperature, we effectively reduce the temperature effect on the photodiode output electrical signal. This simplifies the 3D surface and removes the need for complex controls to account for the thermal transient that affects spectrum intensity. Previous work by Williams [7] used current, EL intensity, and temperature as the axis for the calibration

surface. This necessitated the need for representative temperature measurement of the diode junction to convert EL intensity to current. However, the work of this thesis uses the duty cycle in the place of temperature. This change arises from the fact that junction temperature is dependent on power dissipation and power dissipation is roughly inversely proportional to the duty cycle. For example, when the duty cycle is high, the off time of the switching element is short. The off time is the portion of the period in which the diode is conducting. Therefore, less power is dissipated in the diode for which results in a lower junction temperature. The reverse is also true. When the duty cycle is low, the conduction time of the diode is longer, therefore, junction temperature is higher. This approach realizes the fact that junction temperature is a byproduct of the duty cycle and can be substituted in place of temperature in the 3D current conversion surface. The duty cycle is easily calculated from the output signal of the second PI. This removes the need for accurate temperature measurement of the diode junction and replaces it with a value inherently generated during operation.

4. Calibration Method

To perform the current sensing calibration, a modified Simulink control scheme is utilized as shown in Figure 32. To create the 3D surface, the electronic load is used in constant current mode. In this mode the load resistance is automatically altered by the electronic load to maintain current at the commanded value. The reference value input is quantized in steps of approximately 20% duty cycle. It is then varied in steps to simulate specific duty cycles and the light intensity is manually recorded. This process is repeated in 0.2 A intervals from 0.8 A–3.2 A and from 20%–80% duty cycle manually inserted into PWM block via external potentiometer. The MATLAB curve fitting tool is then used to generate a 3D current conversion surface as shown in Figure 33.

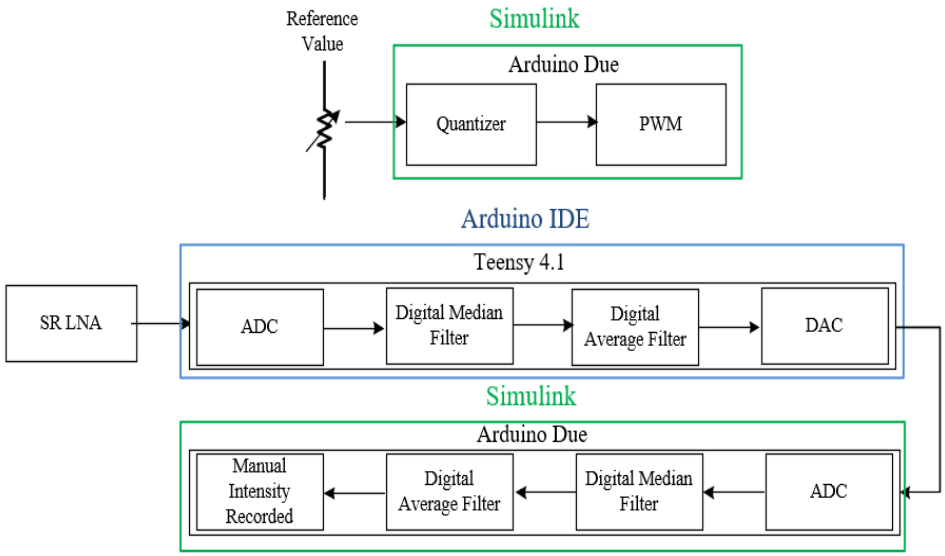

Figure 32. Current Calibration Method

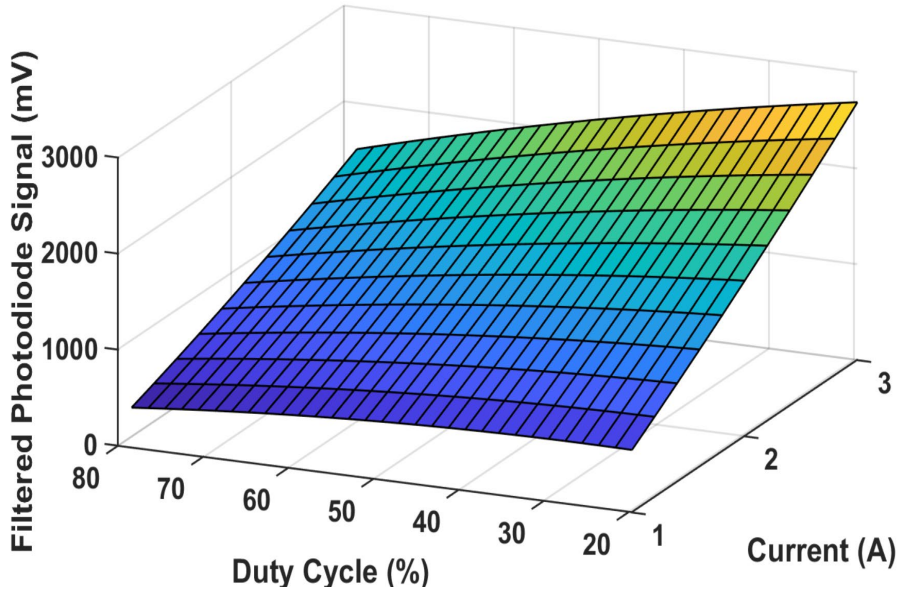

Figure 33. 450 nm Optical High pass Filter Current Conversion Surface

5. Control System Design

The control system was designed and implemented via Simulink with an Arduino Due as the controlling microcontroller. A dual PI average current control scheme was employed in the control system design. The reference voltage was supplied with a potentiometer being powered by the 5 V output pin on the Arduino Due. The resulting voltage divider output was sampled then quantized with the Simulink quantizer block to produce approximately 5 V step changes in reference voltage. The Arduino bias is required when using an Arduino Due in a PI controller scheme. The PI controller drives the error between the commanded value and measured value to zero, and since the Arduino PWM operates with an 8-bit (0–255) input, the PWM output duty cycle would always be zero. Due to this limitation, a bias of 128 is added to the second PI output as shown by Figure 34 to set the initial PWM output duty cycle to 50%.

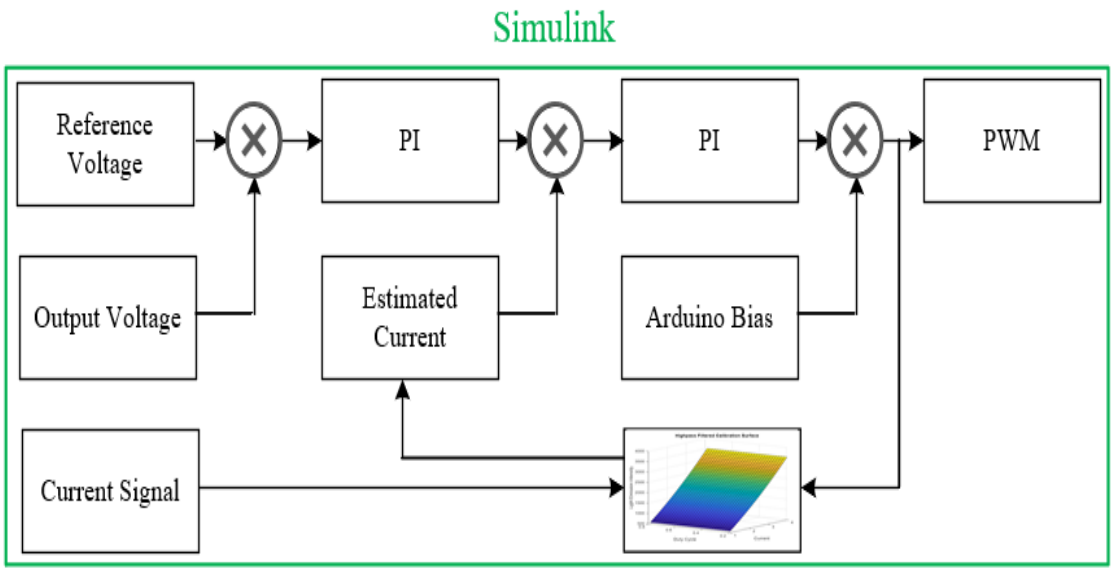

Figure 34. Simplified Control Scheme

The tuning of the PI coefficients was done experimentally utilizing the Ziegler-Nichols method due to the large delays introduced in the filtering process. The polynomial coefficients of the 3D current conversion surface are then used in a Simulink function block as shown in Figure 35 to convert EL and duty cycle into an estimated current in real time.

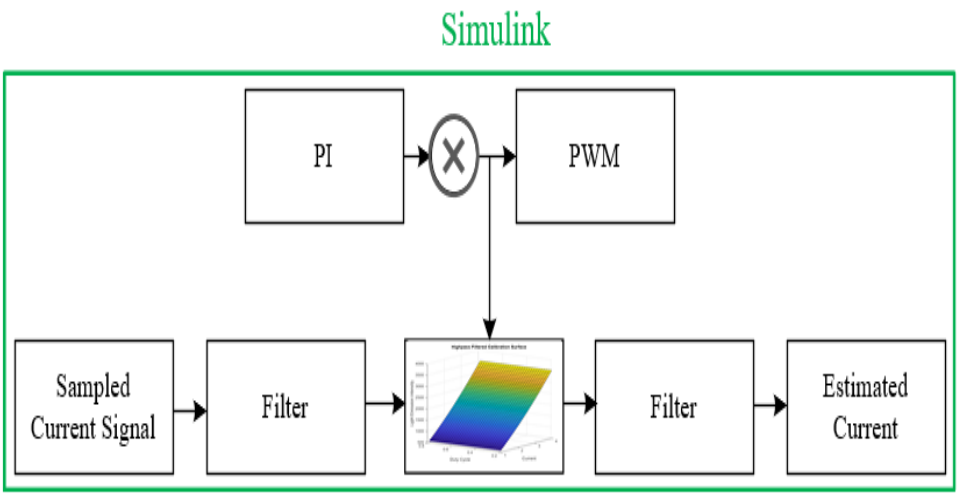

Figure 35. Current Estimation Block Diagram

THIS PAGE INTENTIONALLY LEFT BLANK

IV. TESTING AND ANALYSIS

Before testing, the Simulink current calibration program is executed, and data recorded to generate the current-duty cycle calibration surface within 5% accuracy of the measured current as read on the programmable electronic load. Once the calibration is complete and new polynomial coefficients are uploaded to the buck converter control program, a calibration performance run is performed to ensure the 5% estimated current accuracy is achieved. During the performance run, the output voltage sampling error is recorded and corrected to within 0.1 V of the electronic load and external Fluke 77 III DMM measurements. Once the performance run has been completed satisfactorily within the desired tolerances, the testing plan was initiated. Test 1 and 2 was conducted initially and the calibration data is shown in Table 2 with the calibration surface shown in Figure. 36.

Table 2. Test 1 and 2 Calibration Data

		Reference Step			
		50	100	150	200
Current (A)	1	700.77	517.16	485.00	600.00
	2	1805.00	1396.16	1134.80	1019.00
	3	2347.10	2797.50	2191.70	1455.40

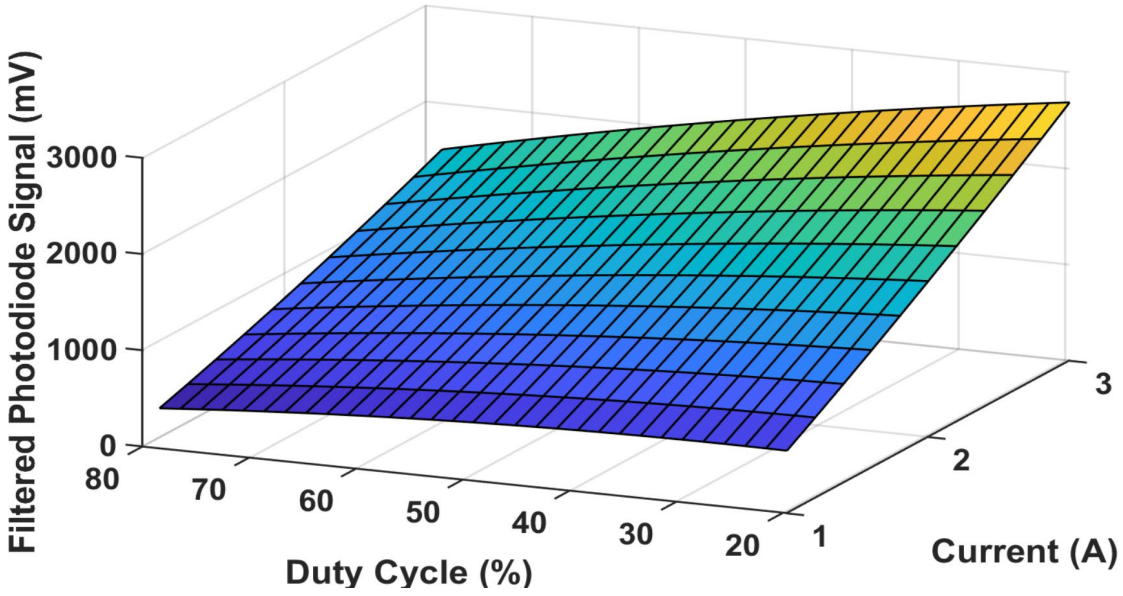

Figure 36. Test 1 and 2 Calibration Surface

Test 3, 4, and 5 utilized a different calibration surface since the testing was conducted several weeks apart with different environmental factors. The calibration data is shown in Table 3 with the calibration surface shown in Figure. 37. Since the prime research objective of this work is to determine a method of extracting real-time converter current utilizing GaN EL, the focus of the test analysis will be estimated current accuracy and estimated current delay time.

Table 3. Test 3, 4, and 5 Calibration Data

		Reference Step			
		50	100	150	200
Current (A)	1	707.00	620.40	534.80	539.30
	2	1852.00	1532.70	1259.30	1010.00
	3	2920.00	2840.70	2241.20	1603.00

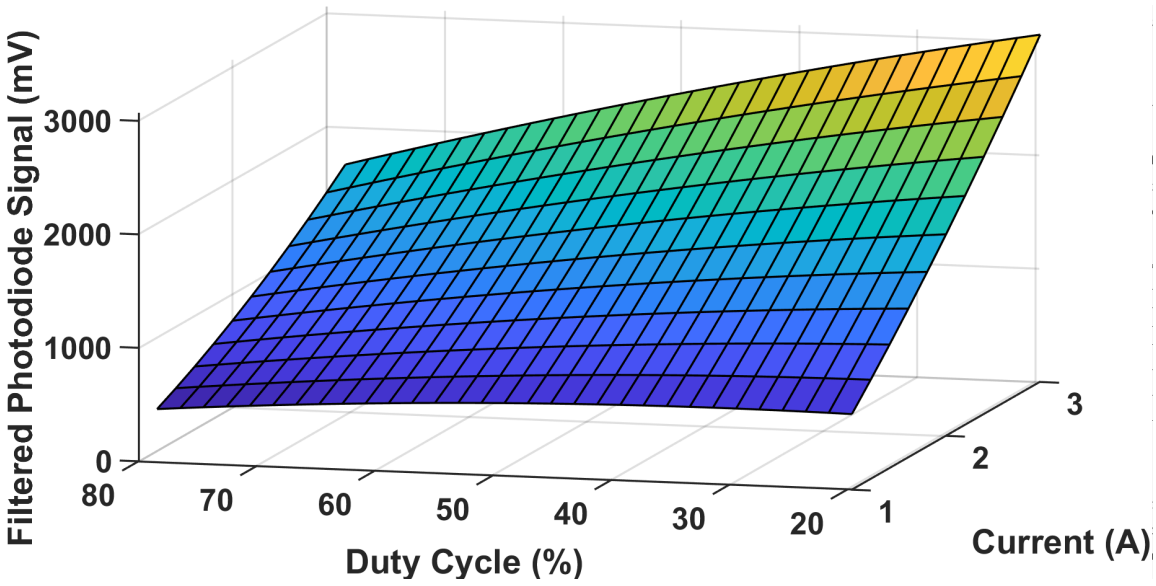

Figure 37. Test 3, 4, and 5 Calibration Surface

A. TEST 1: SMALL VOLTAGE SETPOINT TRANSIENT TEST

The small voltage transient test consisted of a constant 7.2 Ω load established by the programmable electronic load. This resistance was chosen to allow buck converter operation across a wide range of duty cycles yet remain within the 1–3 A calibration range. Since the Arduino control system operates on an 8-bit (0–255) range, the reference values were quantized and step-inserted manually via the voltage reference potentiometer in intervals of 50. Table 4 shows the test sequence of variable voltage reference values inserted.

Table 4. Test 1 Sequence

Step	8-bit Reference	Voltage Equivalent (Volts)
1	100	9.80
2	150	14.71
3	200	19.61
4	150	14.71
5	100	9.80

During the test, the control system was allowed to stabilize before the subsequent step insertion. Commanded current, estimated current, reference voltage, output voltage, and duty cycle were data captured in real-time via Simulink and exported to the MATLAB work area at the conclusion of the test. Output current was calculated with Ohm's law utilizing the output voltage and the programmed load resistance value. Figure 38 shows the output performance of Test 1.

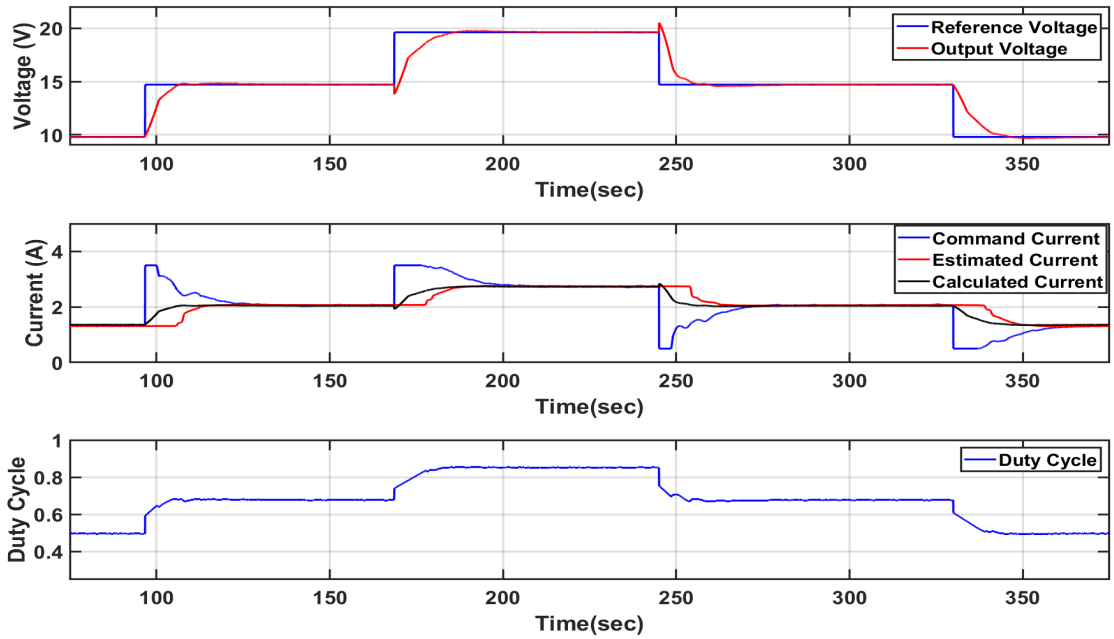

Figure 38. Test 1: 7.2 Ω Constant Load, Variable Reference Voltage

The output voltage during the transient from 14.71 V–19.61 V and from 19.61 V–14.71 V exhibits an instantaneous undershoot and then overshoot. This is due to internal processing of the Arduino controller and the fact that all these traces are recorded therein. A different error correction factor is utilized for different voltage ranges. When the step insertion of the new reference voltage occurs, the error correction value is different, which is represented by an instantaneous voltage change.

During the test, an upper output saturation of 3.5 A and a lower output saturation of 0.5 A were applied to the first PI that generates the commanded current signal. This was done to limit the commanded current overshoot generated due to the delay time between the commanded current step change and the estimated current conversion. As discussed in previous sections, several low-frequency poles were inserted in the form of moving average and median filters to facilitate a semi-stable output signal to accomplish manual calibration.

The large delay time present with an average of 9.05 s in the current system configuration is unacceptable and must be reduced by several orders of magnitude to become a viable current measurement option. The future work section will discuss improvements in design to drastically minimize this effect. Figure 39 shows the accuracy of the estimated current versus the calculated output current. The highest steady-state estimated current error was 3.58%, with an average of 2.0% of calculated output current during the test. The transient current error was much more significant during the test, namely due to the considerable delay time in estimating the diode current. Reducing the current estimation delay time and thus reducing the transient delay error will be the focus of future improvements to this design.

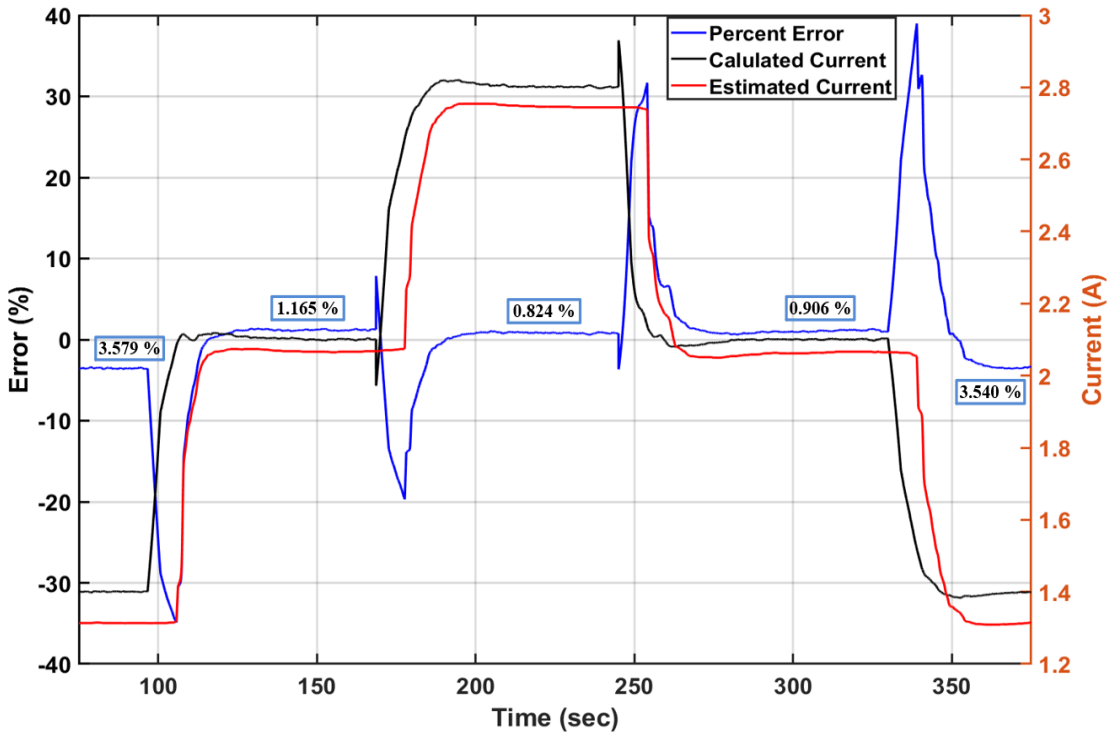

Figure 39. Estimated Current vs. Calculated Current Percent Error

B. TEST 2: LARGE VOLTAGE SETPOINT TRANSIENT TEST

The large voltage transient test consisted of a constant 7.2 Ω load established by the programmable electronic load. Table 5 shows the test sequence of variable voltage reference values inserted. The control system was allowed to stabilize during the test before the subsequent step insertion. Commanded current, estimated current, reference voltage, output voltage, and duty cycle were captured in real-time via Simulink and exported to the MATLAB work area after the test. Output current was calculated with Ohm's law utilizing the output voltage and the programmed load resistance value. Figure 40 shows the output performance of Test 2.

Table 5. Test 2 Sequence

Step	8-bit Reference	Voltage Equivalent (Volts)
1	100	9.80
2	200	19.61
3	100	9.80

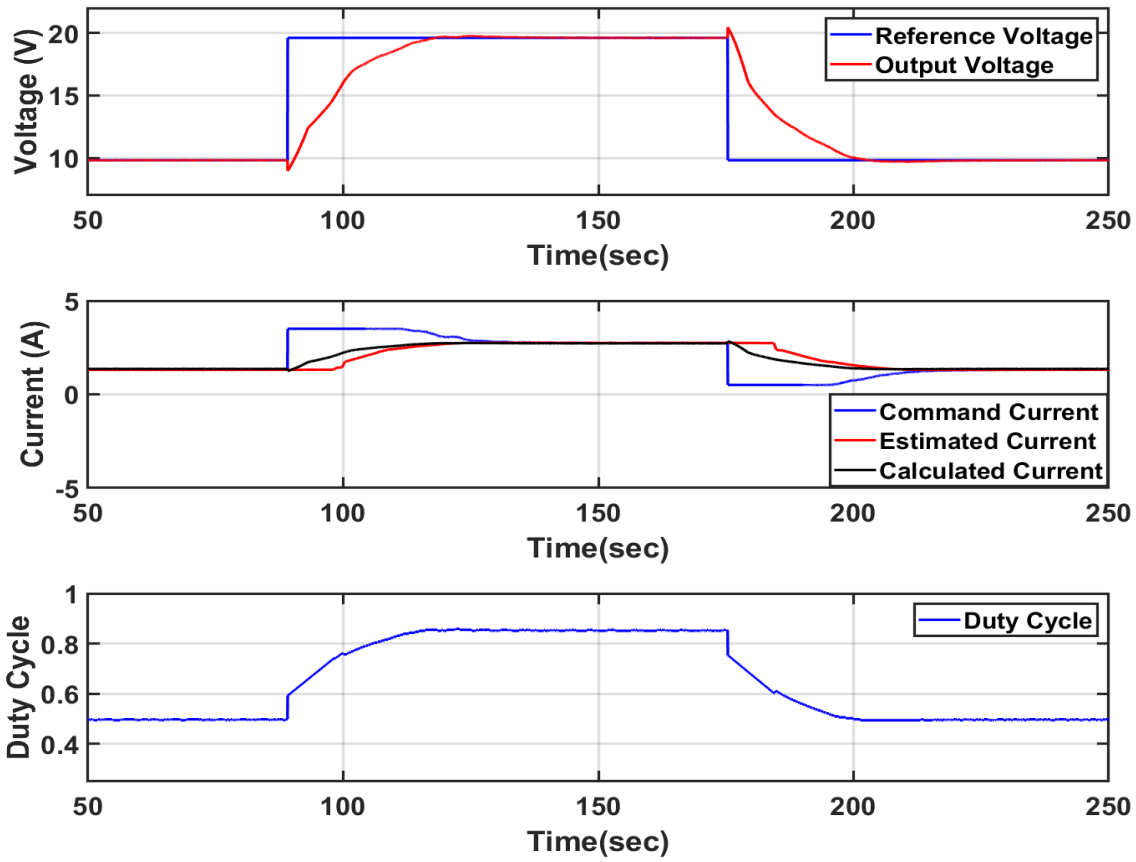

Figure 40. Test 2: 7.2 Ω Constant Load, Variable Reference Voltage

The output voltage from 9.80 V–19.61 V and 19.61 V–9.80 V exhibits the same undershoot and then overshoot as in Test 1. The first PI output saturation was maintained at 3.5 A for the upper output saturation and 0.5 A for the lower saturation, as in Test 1.

The large voltage transient resulted in an average delay time of 9.04 s. This delay time is in line with the average delay time in Test 1. This shows that delay time is not drastically affected by the transient size but is due to the delay introduced by many filters in the processing path creating a constant signal during calibration. Figure 41 shows the accuracy of the estimated current versus the calculated output current. The highest steady-state estimated current error was 3.765%, with an average of 2.8% of calculated output current during the test. The large transient current error is due to the same mechanism as Test 1.

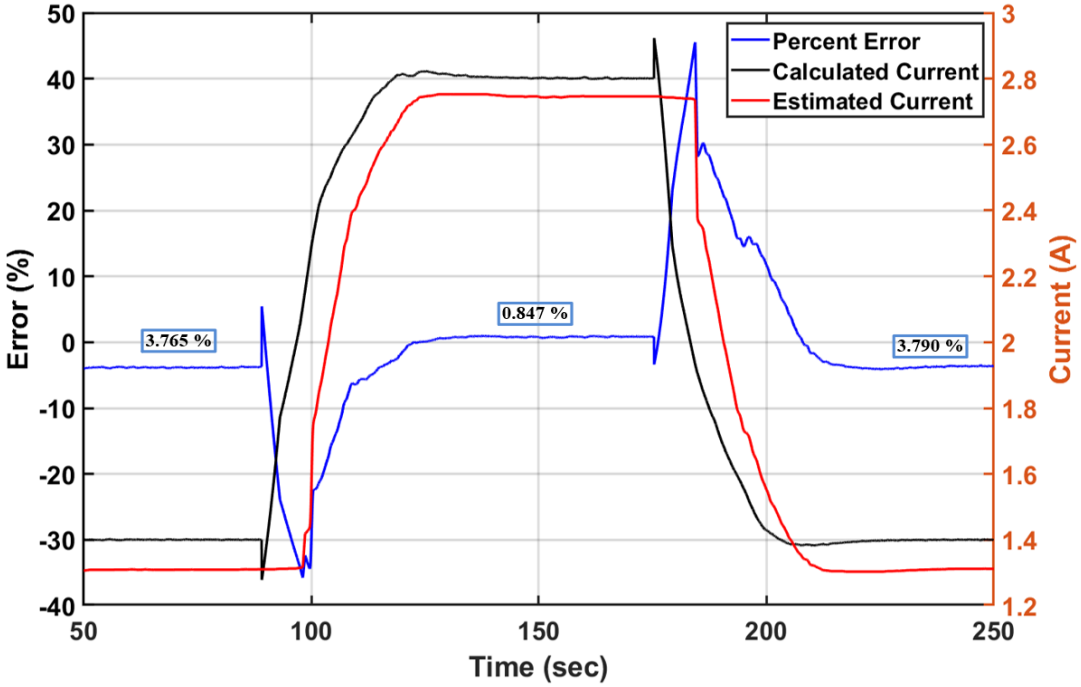

Figure 41. Estimated Current vs. Calculated Current Percent Error

C. TEST 3: LOAD-STEP TRANSIENT TEST

The load-step transient test consisted of a constant 14.71 V reference voltage with three variable load resistances steps inserted at the transient times via the programmable electronic load, as shown in Table 6. The three load resistances step values were chosen based on the value of the constant reference voltage to ensure the buck converter output current remained within the 1–3 A calibration range. The control system was allowed to

stabilize during the test before the subsequent step insertion. Commanded current, estimated current, reference voltage, output voltage, and duty cycle were captured in real-time via Simulink and exported to the MATLAB work area after the test. Output current was calculated with Ohm's law utilizing the output voltage and the programmed load resistance value. Figure 42 shows the output performance of Test 3. Unlike the previous test, no output saturation of the first PI was utilized during this test.

Table 6. Test 3 Sequence

Step	Load Resistance (Ω)
1	15.0
2	7.5
3	4.9
4	7.5
5	15.0

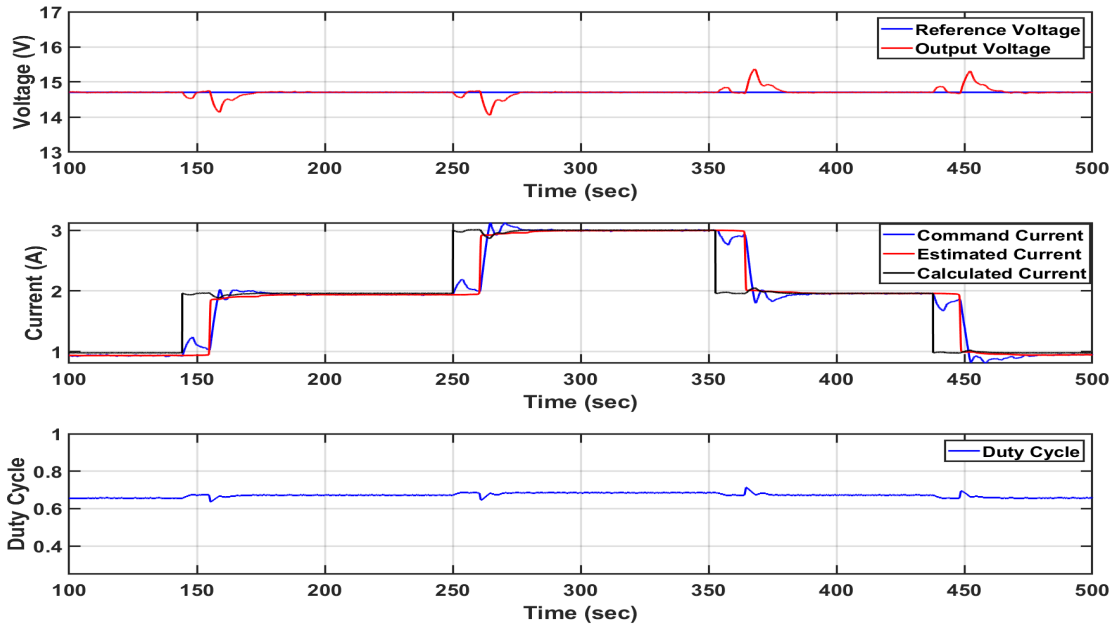

Figure 42. Test 3: 14.71 V Constant Reference Voltage, Variable Load

The current transient test resulted in an average delay time of 10.49 s. Figure 43 shows the accuracy of the estimated current versus the calculated output current. The highest steady-state estimated current error was 4.637%, with an average of 1.96% of calculated output current during the test. The significant transient current error is due to the exact mechanism of the previous test.

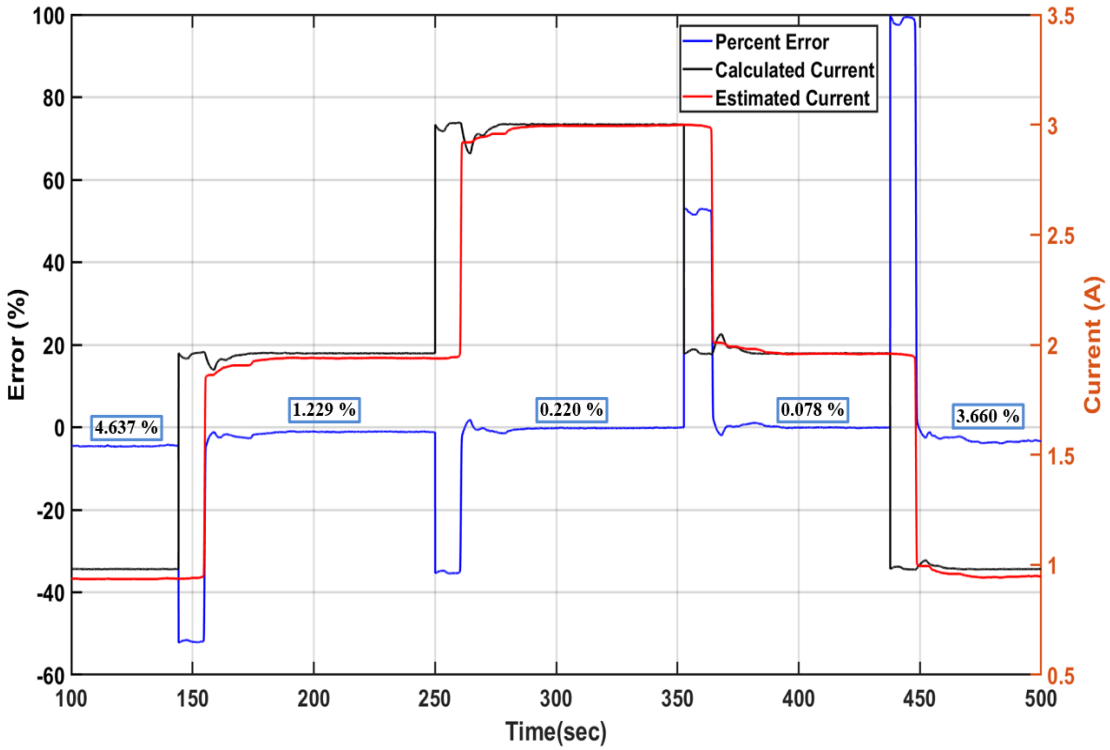

Figure 43. Estimated Current vs. Calculated Current Percent Error

D. TEST 4: SINGLE PI DIRECT CURRENT CONTROL TEST

For Test 4, a modified control program was utilized that eliminated the first PI controller to allow a constant current value manually inserted via the reference potentiometer, as shown in Figure 44. During this test, a constant 4 Ω load was established via the electronic load. The load resistance was chosen to show buck converter operation across a wide array of duty cycles yet maintain the output voltage within the 0–25V design

range. Reference current was varied in accordance with Table 7, and the system was allowed to stabilize prior to the next step insertion.

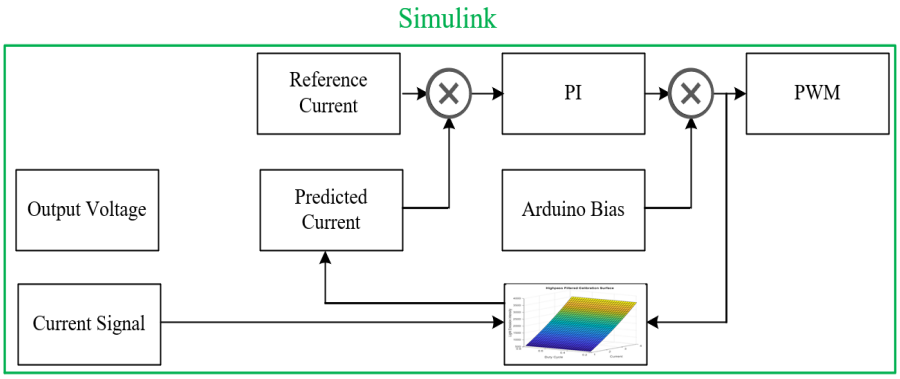

Figure 44. Test 4 Modified Control Program

Table 7. Test 4 Sequence

Step	Reference Current (A)
1	1
2	2
3	3
4	2
5	1

Commanded current, estimated current, reference voltage, output voltage, and duty cycle were captured in real-time via Simulink and exported to the MATLAB work area after the test. Output current was calculated with Ohm's law utilizing the output voltage and the programmed load resistance value. Figure 45 shows the output performance of Test 4.

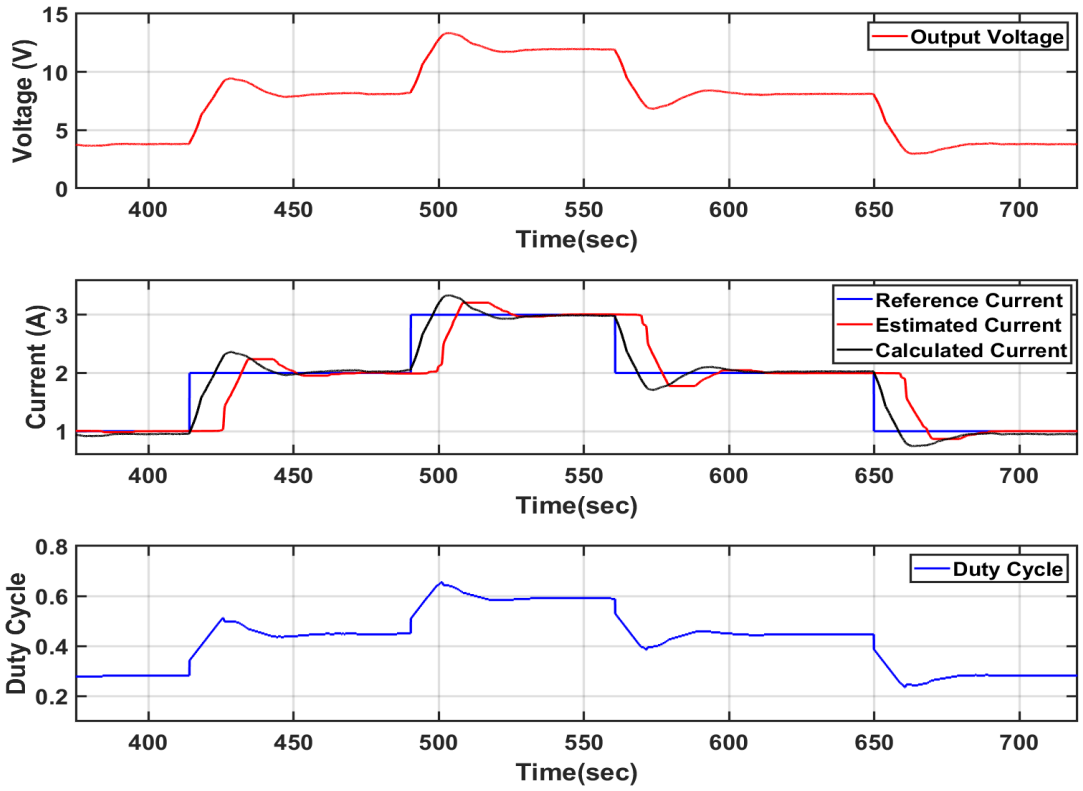

Figure 45. Test 4: Single PI, Constant Load, Variable Reference Current

No PI output saturation was utilized during this test. The clipping estimated current exhibited during the transients is due to the large window median filter used to reduce the duty cycle dependency of the EL intensity. This effect can be eliminated and discussed in the future work section. The current transient test resulted in an average delay time of 9.58 s. Figure 46 shows the accuracy of the estimated current versus the calculated output current. The highest steady-state estimated current error was 4.93%, with an average of 2.78% of calculated output current during the test. The large transient current error is due to the same mechanism as the previous test.

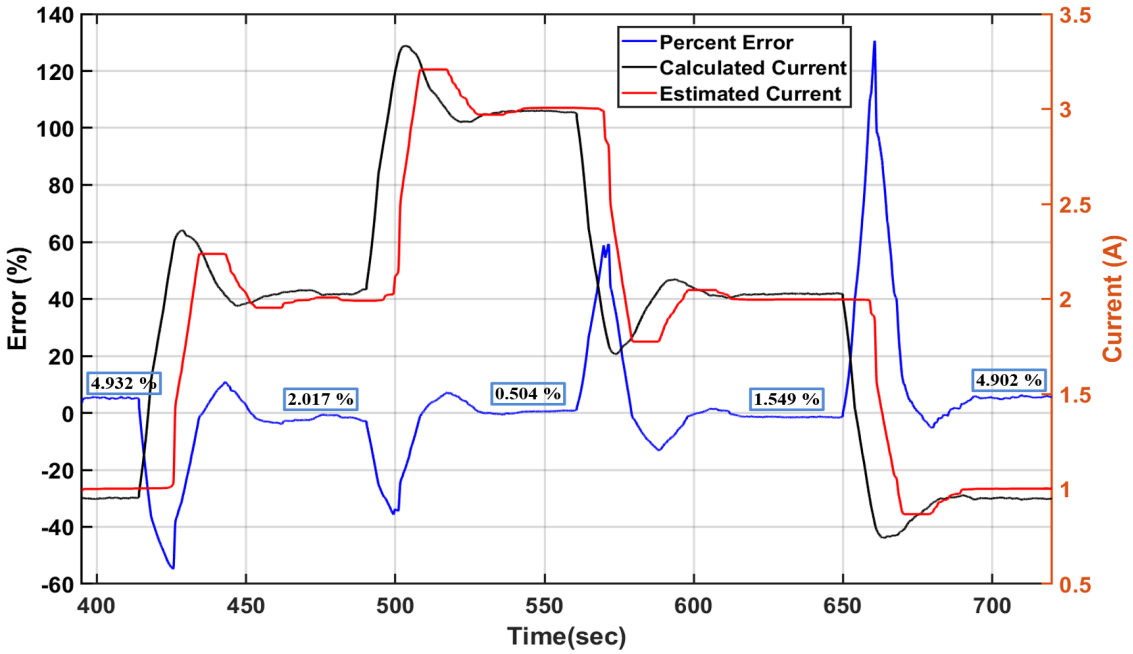

Figure 46. Estimated Current vs. Predicted Current Percent Error

E. TEST 5: ACCURACY AND STABILITY TEST

For the accuracy and stability test, the original dual PI control program was used. A constant 14.71 V reference voltage was inserted, with a constant load resistance of 7.5 Ω established via the electronic load. No variables were changed, and the buck converter was allowed to operate in steady-state for approximately one hour. Commanded current, estimated current, reference voltage, output voltage, and duty cycle were captured in real-time via Simulink and exported to the MATLAB work area after the test. Output current was calculated with Ohm's law utilizing the output voltage and the programmed load resistance value. Figure 47 shows the output performance of Test 5. No PI output saturation was utilized during this test. This test demonstrates that the current conversion method is stable, accurate, and can be employed continuously without breakdown. Figure 48 shows the highest steady-state estimated current error was 0.481%, with an average of 0.380% of calculated output current during the test.

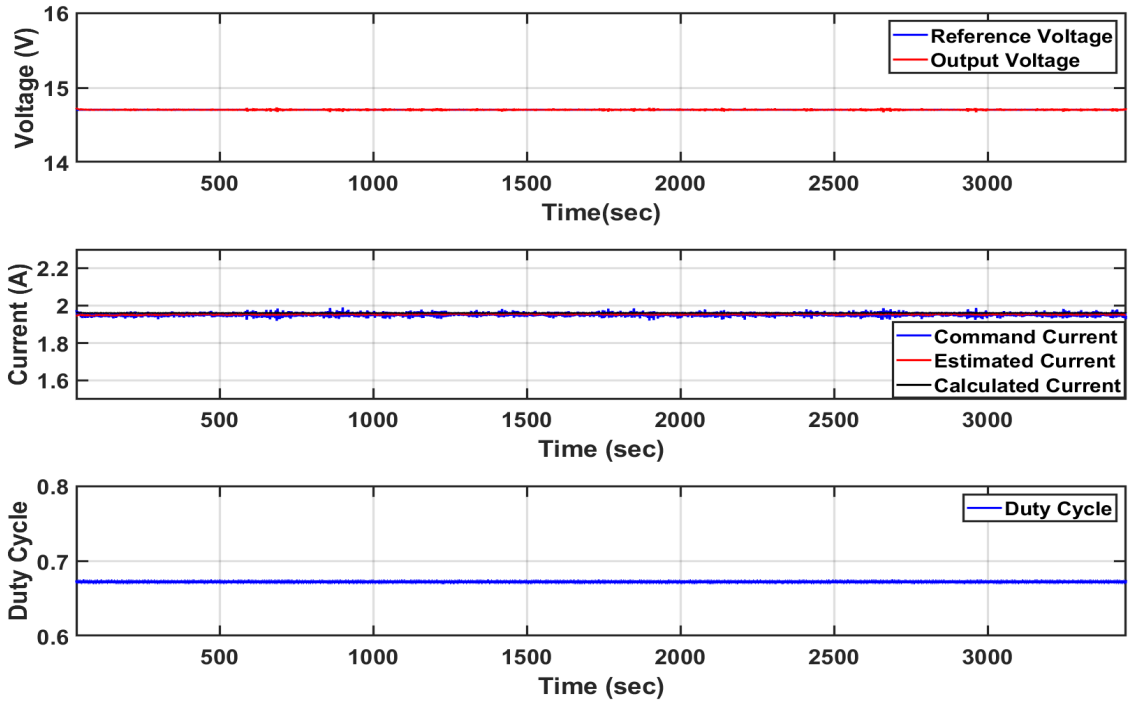

Figure 47. Test 5: 14.71 V Constant Reference Voltage, Constant 7.5 Ω Load

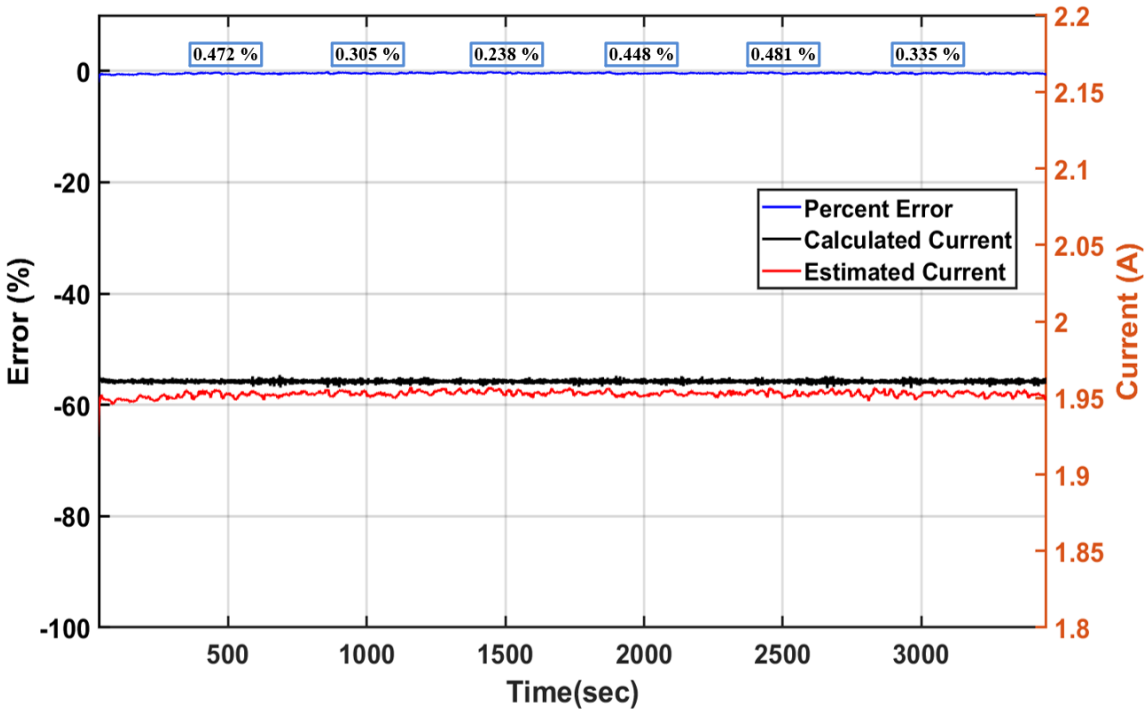

Figure 48. Estimated Current vs. Calculated Current Percent Error

V. CONCLUSION AND FUTURE WORK

A. CONCLUSION

This research investigated the feasibility of real-time control of the current mode buck converter via a vertical GaN PN diode electroluminescence (EL). A current mode asynchronous buck converter was designed and built to remain in continuous-conduction mode (CCM) under all load conditions to ensure maximum diode conduction time. The GaN diode EL was optically filtered and converted into an electrical signal. The electrical waveform was further digitally filtered and then converted into an estimated current value as a function of EL intensity and buck converter duty cycle. The estimated current value was utilized for the inner loop feedback. Five tests were performed to test the estimated current accuracy and estimated current delay time. The average delay time across the first four tests was 9.54 s. Modern dc–dc converters have sub-millisecond response times, so improving this metric must be the focus of future optimization. The estimated current accuracy across the five tests was 2.02%, well within the 5% initial design specification. The manual calibration method to achieve this accuracy level caused much of the current delay due to the need for extensive digital filtering to create a stable current signal.

B. FUTURE WORK

The delay time in the current response can be reduced with specialized hardware selection and a low-overhead programming language. The Arduino Due was selected since it had the highest capability of the Arduinos supported by Simulink. However, the ADC bandwidth was inadequate due to the number of signals to be sampled and the buck converter switching frequency. The need to add a secondary microcontroller for dedicated sampling and initial DSP of the photodiode current signal drastically increased the current delay time. Simulink has many advantages that facilitate rapid programming. However, due to the graphical nature of the programming language, it has a much higher overhead when compared to Python or C-based languages. Optimization of both the hardware and coding will be required to obtain sub-millisecond or better current estimation times. Additionally, the current estimation accuracy and current delay would benefit from a more

sophisticated sampling and filtering process. The use of median filters to remove the duty cycle dependence and multiple moving average filters to remove EMI noise directly contribute to the process delay time of the current signal.

Since the optical coupling is in an open atmosphere, environmental effects such as humidity need to be further investigated. Whereas comprehensive testing of this phenomenon was not an objective in this research, it was noted during testing that humidity fluctuations affected the intensity of the GaN EL and the accuracy of the calibration surface. A proposed solution to eliminate this interference would be to place the GaN test device in a humidity-sealed enclosure or directly butt couple the fiber to the device and encapsulate the diode rather than leave it open to the environment.

APPENDIX: SIMULINK/MATLAB

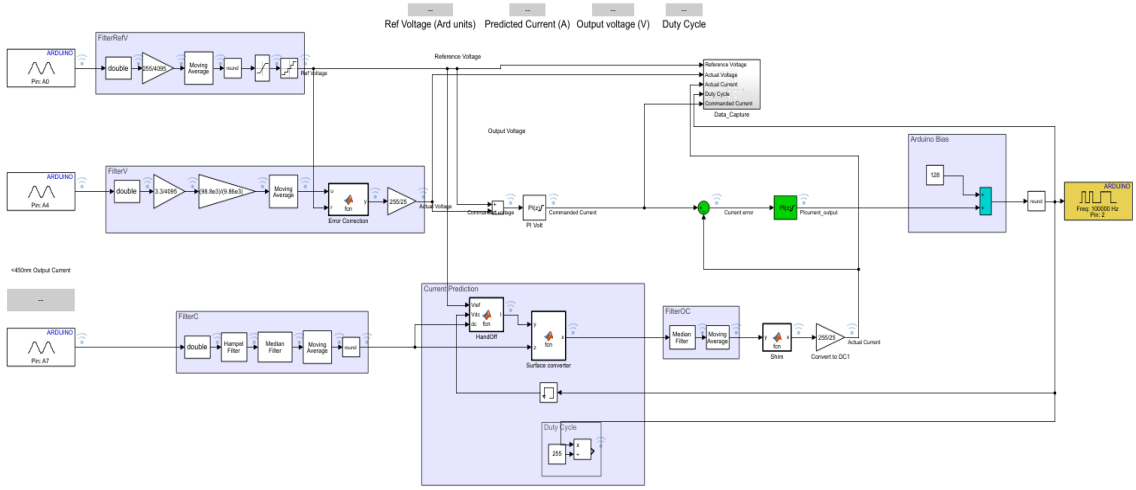

Figure 49. Simulink Dual PI Control Program

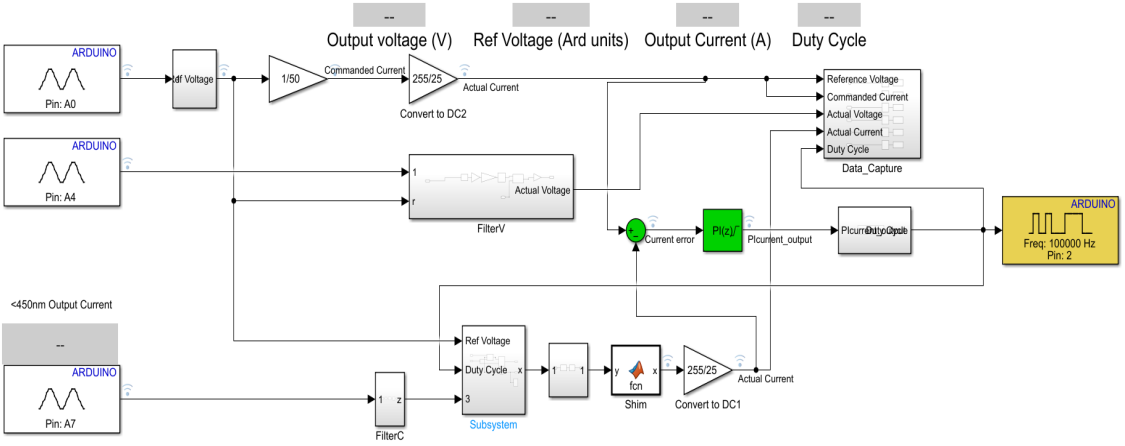

Figure 50. Simulink Single PI Control Program

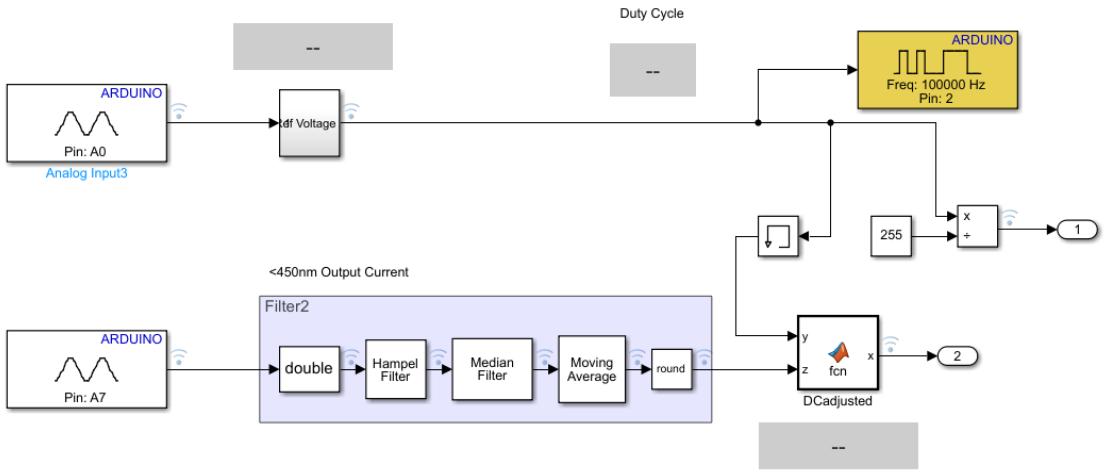

Figure 51. Simulink Calibration Program

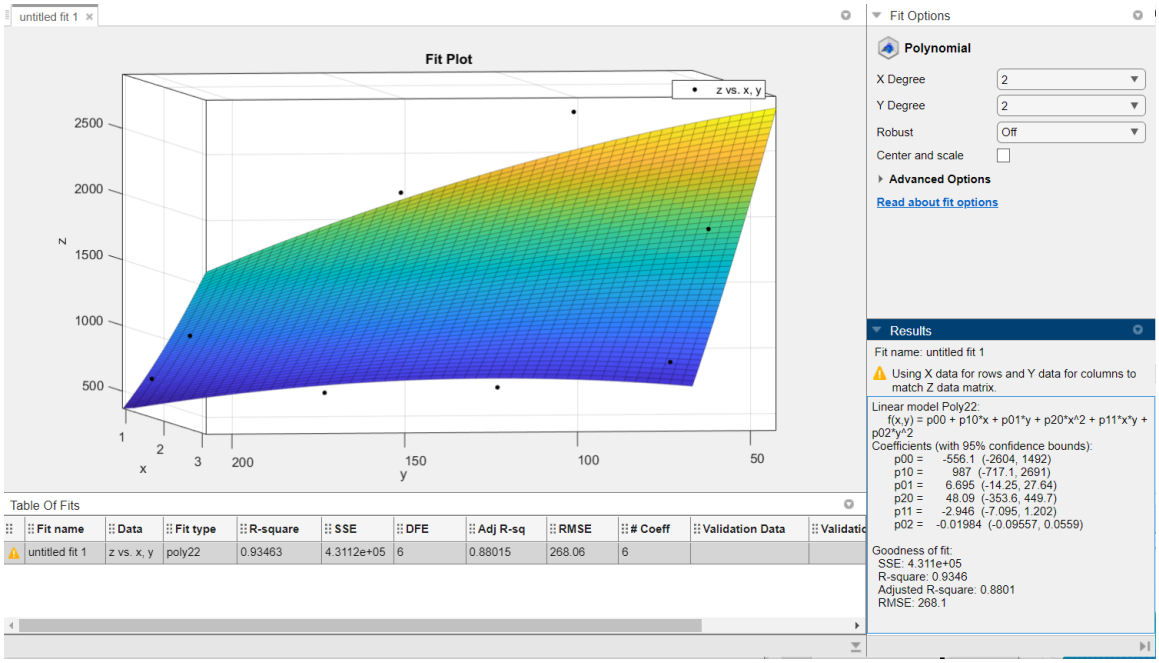

Figure 52. MATLAB Curve Fitting Tool Test 1 and 2 Calibration Surface

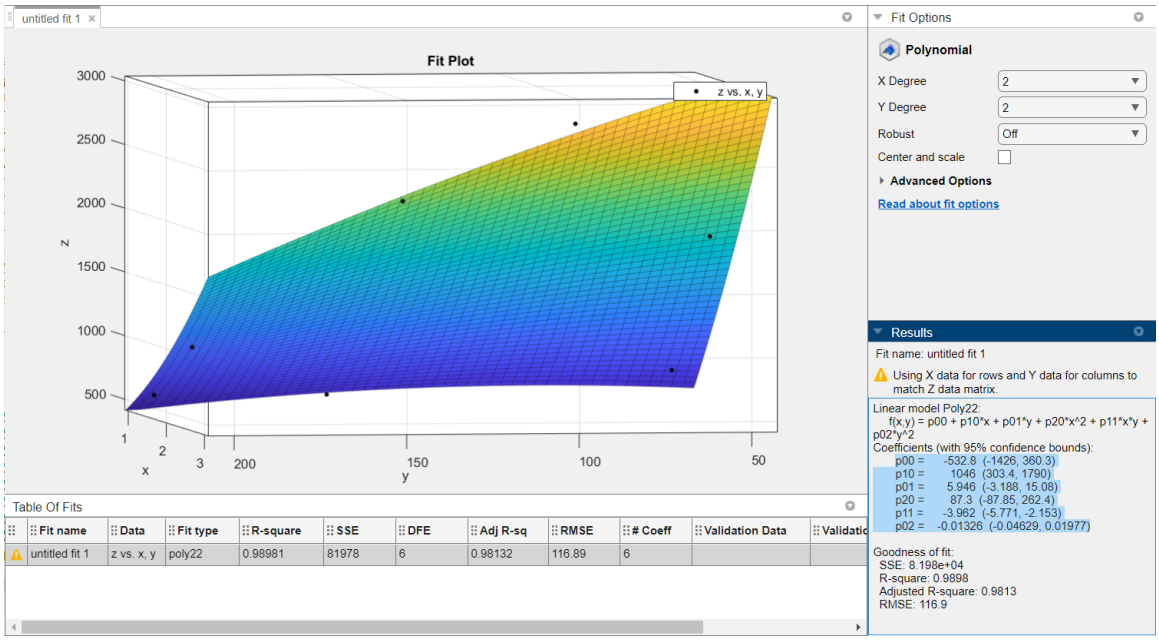

Figure 53. MATLAB Curve Fitting Tool Test 3, 4, and 5 Calibration Surface

THIS PAGE INTENTIONALLY LEFT BLANK

LIST OF REFERENCES

[1] K. Osborn, "The AN/SPY-6 is the radar system of the future," *The National Interest*, Feb. 09, 2022. https://nationalinterest.org/blog/buzz/anspy-6-radar-system-future-200477 (accessed Oct. 11, 2022).

[2] Lockheed Martin, "U.S. army awards Lockheed Martin contract extending AN/TPQ-53 radar range," *Media - Lockheed Martin*, Oct. 2018. https://news.lockheedmartin.com/2018-10-08-U-S-Army-Awards-Lockheed-Martin-Contract-Extending-AN-TPQ-53-Radar-Range (accessed Oct. 11, 2022).

[3] S. Kalker, C. H. van der Broeck, L. A. Ruppert, and R. W. De Doncker, "Next Generation Monitoring of SiC mosfets Via Spectral Electroluminescence Sensing," *IEEE Trans. Ind. Appl.*, vol. 57, no. 3, pp. 2746–2757, 2021.

[4] C. Li, Z. Lu, H. Wu, W. Li, X. He, and S. Li, "Junction Temperature Measurement Based on Electroluminescence Effect in Body Diode of SiC Power MOSFET," in *2019 IEEE Applied Power Electronics Conference and Exposition (APEC)*, 2019, pp. 338–343.

[5] M. Broeg, "Current and temperature sensing via light emission from GaN PN junctions," M.S. thesis, Dept. of Elec. and Comp. Eng., NPS, Monterey, CA, USA, 2019.

[6] C. Robinson, "Electrooptical characteristics of SiC MOSFET body diode and GaN power diode," M.S. thesis, Dept. of Elec. and Comp. Eng., NPS, Monterey, CA, USA, 2022.

[7] J. L. Williams, "GaN light emission for control system feedback," M.S. thesis, Dept. of Elec. and Comp. Eng., NPS, Monterey, CA, USA, 2020. [Online]. Available: http://hdl.handle.net/10945/70788

[8] Microchip, "Synchronous Buck Converter Overview – Developer Help." https://microchipdeveloper.com/desanl:synchronous-buck-converter-overview (accessed Oct. 12, 2022).

[9] J. Shepard, "How to Quickly Implement Buck Converters for Factory Automation, 5G, and the IoT," *Digi-Key Electronics*, May 24, 2022. https://www.digikey.com/en/articles/how-to-quickly-implement-buck-converters-for-factory-automation-5g-iot (accessed Oct. 12, 2022).

[10] Richtek, "Reducing EMI in buck converters | Richtek Technology." https://www.richtek.com/Design%20Support/Technical%20Document/AN045 (accessed Oct. 12, 2022).

[11] N. Mohan, T. M. Undeland, and W. P. Robbins, *Power Electronics: Converters, Applications, and Design*, 2nd ed. Hoboken, NJ, USA: John Wiley & Sons, 2003.

[12] P. A. Bindra, "Improved voltage-mode control scheme enhances buck converters jitter performance at high frequency," *Digi-Key Electronics*, Nov. 05, 2013. https://www.digikey.com/es/articles/improved-voltage-mode-control-scheme-enhances-buck-converters-jitter-performance-at-high-frequency (accessed Oct. 12, 2022).

[13] S. Keeping, "Voltage and current-mode control for PWM signal generation in DC-to-DC switching regulators," *Digi-Key Electronics*, Oct. 01, 2014. https://www.digikey.com/en/articles/voltage-and-current-mode-control-for-pwm-signal-generation-in-dc-to-dc-switching-regulators (accessed Oct. 11, 2022).

[14] Microchip, "Buck converter average current mode," *Microchip Technology*. https://skills.microchip.com/digital-control-techniques-for-power-converters-using-dspic-dsc/698468 (accessed Oct. 12, 2022).

[15] L. H. Dixon, *Average current mode control of switching power supplies*, Unitrode, SEM 700, 1990.

[16] Y. Wang, J.-G. Liu, J. Zhao, and Y. Yang, "Split Core Closed Loop Hall Effect Current Sensors and Applications," Nuremburg, Germany, May 2012, pp. 1633–1638. doi: 10.13140/2.1.1422.2727.

[17] M. Soltero, "What is a Hall-effect sensor?," May 17, 2021. https://e2e.ti.com/blogs_/b/analogwire/posts/what-is-a-hall-effect-sensor (accessed Oct. 12, 2022).

[18] O. Aiello, P. Crovetti, and F. Fiori, "Investigation on the susceptibility of hall-effect current sensors to EMI," in *10th International Symposium on Electromagnetic Compatibility*, 2011, pp. 368–372.

[19] K. Nelkovski, "A GaN Roundup: RF MMICs, Power ICs, and SOIC Drivers Keep the Ball Rolling – News," *All about circuits*, Dec. 22, 2021. https://www.allaboutcircuits.com/news/a-gallium-nitride-roundup-rf-mmic-power-ic-and-soic-drivers-keep-ball-rolling/ (accessed Oct. 11, 2022).

[20] Navitas, "Introduction to wide bandgap semiconductors | Navitas." https://navitassemi.com/introduction-to-wide-bandgap-semiconductors/ (accessed Oct. 12, 2022).

[21] B. J. Baliga, *Fundamentals of Power Semiconductor Devices*, 2nd ed. New York, NY, USA: Springer, 2010. [Online]. Available: https://books.google.com/books?id=UiqrUWrYZXkC

[22] J. L. Hudgins, G. S. Simin, E. Santi, and M. A. Khan, "An assessment of wide bandgap semiconductors for power devices," *IEEE Trans. Power Electron.*, vol. 18, no. 3, pp. 907–914, 2003.

[23] D. Neamen, *Semiconductor Physics And Devices*, 4th ed. New York, NY, USA: McGraw-Hill Higher Education, 2011. [Online]. Available: https://books.google.com.ai/books?id=R_xKAgAAQBAJ

[24] Y. Zhang, "Comparison between competing requirements of GaN and SiC family of power switching devices," *IOP Conf. Ser. Mater. Sci. Eng.*, vol. 738, no. 1, 2020, doi: 10.1088/1757-899X/738/1/012004.

[25] electrical4u, "Reverse Recovery Time of Diode | Electrical4U," Oct. 28, 2020. https://www.electrical4u.com/reverse-recovery-time-of-diode/ (accessed Oct. 11, 2022).

[26] M. Alam, "ECE 606 lecture 13: Recombination-generation," *Nanohub Purdue Univ.*, Feb. 2009, doi: https://nanohub.org/resources/5807.

[27] K. Knowles, C. Dunleavy, and D. Brook, "Direct and indirect band gap semiconductors," *Direct and Indirect Band Gap Semiconductors*. https://www.doitpoms.ac.uk/tlplib/semiconductors/direct.php (accessed Oct. 12, 2022).

[28] F. Rana, "Lecture, topic: 'Optical transitions in bulk semiconductors.' ECE5330." Cornell University, Ithaca, NY, 2019. [Online]. Available: https://courses.cit.cornell.edu/ece533/Lectures/handout3.pdf

[29] S. Kavanagh, "A study focusing on the effects of HTOL stress on the luminescence spectrum of GaN diodes to characterize component degradation," M.S. thesis, Dept. of Elec. and Comp. Eng., NPS, Monterey, CA, USA, 2022.

[30] M. A. Porter, J. Williams, M. Broeg, K. Corzine, and T. Weatherford, "Current and temperature measurement via spectral decomposition of light emission from a GaN power diode," in *2020 IEEE Applied Power Electronics Conference and Exposition (APEC)*, 2020, pp. 640–646. doi: 10.1109/APEC39645.2020.9124317.

[31] Arrow, "KIT8020-CRD-8FF1217P-1 reference design | DC to DC single output power supplies," *Arrow*. https://www.arrow.com/en/reference-designs/kit8020-crd-8ff1217p-1-silicon-carbide-mosfet-evaluation-kit/06bdc7bf3263d7fd75dd431fce4446da (accessed Oct. 12, 2022).

[32] Arduino, "Arduino Due," Arduino Online Shop. https://store-usa.arduino.cc/products/arduino-due (accessed Oct. 12, 2022).

[33] PJRC, "Teensy® 4.1 development board," Jun. 19, 2022. https://www.pjrc.com/store/teensy41.html (accessed Oct. 12, 2022).

THIS PAGE INTENTIONALLY LEFT BLANK

INITIAL DISTRIBUTION LIST

1. Defense Technical Information Center
   Ft. Belvoir, Virginia

2. Dudley Knox Library
   Naval Postgraduate School
   Monterey, California